

Unconventional states of bosons with the synthetic spin–orbit coupling

This article has been downloaded from IOPscience. Please scroll down to see the full text article.

2013 J. Phys. B: At. Mol. Opt. Phys. 46 134001

(<http://iopscience.iop.org/0953-4075/46/13/134001>)

View [the table of contents for this issue](#), or go to the [journal homepage](#) for more

Download details:

IP Address: 110.200.0.132

The article was downloaded on 24/06/2013 at 14:23

Please note that [terms and conditions apply](#).

REVIEW ARTICLE

Unconventional states of bosons with the synthetic spin–orbit coupling

Xiangfa Zhou¹, Yi Li², Zi Cai³ and Congjun Wu²¹ Key Laboratory of Quantum Information, University of Science and Technology of China, CAS, Hefei, Anhui 230026, People's Republic of China² Department of Physics, University of California, San Diego, CA 92093, USA³ Physics Department, Arnold Sommerfeld Center for Theoretical Physics, and Center for NanoScience, Ludwig-Maximilians-Universität München, D-80333 München, GermanyE-mail: xfzhou@ustc.edu.cn and wucj@physics.ucsd.edu

Received 21 January 2013, in final form 26 March 2013

Published 24 June 2013

Online at stacks.iop.org/JPhysB/46/134001**Abstract**

The spin–orbit coupling with bosons gives rise to novel properties that are absent in usual bosonic systems. Under very general conditions, the conventional ground state wavefunctions of bosons are constrained by the ‘no-node’ theorem to be positive definite. In contrast, the linear dependence of the spin–orbit coupling leads to complex-valued condensate wavefunctions beyond this theorem. In this paper, we review the study of this class of unconventional Bose–Einstein condensations focusing on their topological properties. Both the 2D Rashba and 3D $\vec{\sigma} \cdot \vec{p}$ -type Weyl spin–orbit couplings give rise to Landau-level-like quantization of single-particle levels in the harmonic trap. Interacting condensates develop the half-quantum vortex structure spontaneously breaking the time-reversal symmetry and exhibit topological spin textures of the skyrmion type. In particular, the 3D Weyl coupling generates topological defects in the quaternionic phase space as an SU(2) generalization of the usual U(1) vortices. Rotating spin–orbit-coupled condensates exhibit rich vortex structures due to the interplay between vorticity and spin texture. In the Mott-insulating states in optical lattices, quantum magnetism is characterized by the Dzyaloshinskii–Moriya-type exchange interactions.

(Some figures may appear in colour only in the online journal)

1. Introduction

The spin–orbit (SO) coupling plays an important role in the interdisciplinary areas of physics. In quantum mechanics, the SO coupling arises from the relativistic effect as a low-energy approximation to the Dirac equation. Its semi-classic picture is the Thomas precession that electron spin moment couples to a velocity-dependent effective magnetic field generated by the Lorentz transformation of the electric field. In atomic physics, the SO coupling constitutes one of the basic elements to the formation of the atomic structures. The development in condensed matter physics shows that the SO coupling is indispensable for important phenomena ranging from spintronics [1], anomalous Hall effects [2, 3], spin Hall

effects [4–7], to topological insulators [8, 9]. In particular, topological insulators have become a major research focus of current condensed matter physics.

Most current studies of the SO coupling are considered for fermionic systems of electrons. On the other hand, the ultracold atomic systems have opened up a whole new opportunity to explore novel states of matter that are not easily accessible in usual condensed matter systems. In particular, it currently becomes experimentally possible to implement various kinds of SO-coupled Hamiltonians in ultracold atomic gases for both fermions and bosons [10–17]. The high controllability of these systems makes them an ideal platform to explore novel SO-coupled physics with bosons.

An important property of bosons is the ‘no-node’ theorem, which states that in the coordinate representation the many-body ground state wavefunctions are positive definite [18]. This theorem is valid under very general conditions such as the Laplacian-type kinetic energy, arbitrary single-particle potentials and coordinate-dependent two-body interactions. It applies to most of the known ground states of bosons, including Bose–Einstein condensations (BECs), Mott insulators and supersolids. Technically, it indicates that the ground state wavefunctions of bosons can be reduced to positive-definite distributions, and thus imposes a strong constraint on bosonic states. For example, it rules out the possibility of time-reversal (TR) symmetry breaking ground states in traditional boson systems. Considerable efforts have been made in exploring unconventional BECs beyond the ‘no-node’ theorem [19]. One way is the meta-stable state of bosons in high orbital bands in optical lattices [20–23], because the ‘no-node’ theorem does not apply to excited states. Unconventional BECs with complex-valued condensate wavefunctions have been experimentally realized [24–26].

The kinetic energies of SO-coupled systems are no longer Laplacian but linearly depend on momentum, which invalidates the necessary conditions for the ‘no-node’ theorem as pointed out in [19]. This provides another way towards unconventional BECs. For instance, the Rashba SO-coupled BECs were early investigated for both isotropic [27] and anisotropic cases [28]. In the isotropic case, the Rashba coupling leads to degenerate single-particle ground states along a ring in momentum space whose radius k_{so} is proportional to the SO coupling strength. Such a momentum scale is absent in usual BECs in which bosons are condensed to the zero momentum state, and thus bears certain similarities to Fermi momentum in fermion systems. If the interaction is spin-independent, then the condensates are frustrated in the free space at the Hartree–Fock level, and quantum zero-point energy selects a spin-spiral state based on the ‘order-from-disorder’ mechanism. Imposing the trapping potential further quantizes the motion around the SO ring which leads to Landau-level-type quantization of the single-particle levels. Under interactions, condensates spontaneously break the TR symmetry exhibiting topologically non-trivial spin textures of the skyrmion type [27]. All of these features are beyond the framework of the ‘no-node’ theorem.

Recently, SO-coupled systems with ultra-cold bosons have aroused a great deal of research interest in both experiment and theory [10]. Experimentally, pioneered by Spielman’s group [11–13], BECs with SO coupling in the anisotropic 1D limit have been realized by engineering the atom–laser interactions through Raman processes [11–16]. Condensations at finite momenta and exotic spin dynamics have been observed [11–17]. Various experimental schemes have been proposed to realize the isotropic Rashba SO coupling [29–35]. On the side of theory, the Rashba SO-coupled bosons have been extensively investigated under various conditions, including the exotic spin structures in the free space, spin textures in harmonic traps, vortex structures in rotating traps and the SO-coupled quantum magnetism in the Mott-insulating states [28, 27, 38–64]. Furthermore, a recent

progress shows that a 3D $\vec{\sigma} \cdot \vec{p}$ -type SO coupling can also be implemented with atom–laser interactions [65–70]. This is a natural symmetric extension of the Rashba SO coupling to the 3D-dubbed Weyl SO coupling due to its similarity to the relativistic Hamiltonian of Weyl fermions [71]. The Weyl SO-coupled BECs have also been theoretically investigated [66, 72–76].

In addition to the ultra-cold atom systems, recent progress in condensed matter systems has also provided an SO-coupled boson system of excitons. Excitons are composite objects of conduction electrons and valence holes; both of their effective masses are small, and thus relativistic SO coupling exists in their centre-of-mass motion. The effects of the SO coupling on exciton condensations have been theoretically investigated [27, 77], including the spin texture formations [27]. An important experiment progress has been achieved in Butov’s group [78, 79], that spin textures in a cold exciton gas have been observed in GaAs/AlGaAs-coupled quantum wells from the photoluminescence measurement.

In the rest of this paper, we review the current theoretical progress of studying SO-coupled bosons including both the 2D Rashba and 3D Weyl SO couplings. Our emphases will be on the non-trivial topological properties which are absent in conventional BECs. The single-particle spectra will be reviewed in section 2. They exhibit a similar structure to the Landau-level quantization in the sense that the dispersion with the angular momentum is strongly suppressed by SO couplings [27, 41, 42, 45, 53, 65, 72, 80]. However, a crucial difference from the usual magnetic Landau levels is that these SO-coupling-induced Landau levels maintain the TR symmetry, and thus their topology belongs to the Z_2 class [27]. The interplay between interactions and topology gives rise to a variety of topological non-trivial condensate configurations and spin textures, which will be reviewed in section 3. In particular, the 3D condensates with the Weyl coupling exhibit topological defects in the quaternionic phase space. It is exciting to find an application of the beautiful mathematical concept of quaternions. In section 4, we review the SO-coupled BECs in rotating traps, which are subject to both the Abelian vector potential due to the Coriolis force and the non-Abelian one from the SO coupling. The combined effects of the vorticity and spin topology lead to rich structures [81–85], including half-quantum vortex lattices, multi-domain of plane-wave states and giant vortices. In section 5, we summarize the current progress on strongly correlated SO-coupled systems [86–90]. Furthermore, in the strongly correlated Mott insulators, the SO coupling effects exhibit in the quantum magnetism as the Dzyaloshinskii–Moriya-type exchange interactions [91–96], which will be reviewed in section 6. Conclusions and outlooks are presented in section 7.

Due to the rapid increasing literatures and the limit of space, we will not cover other important topics, such as SO-coupled fermions [17, 44, 80, 97–109], SO-coupled dipolar bosons [50, 84] and proposals for experimental implementations [29–37].

2. The SO-coupled single-particle spectra and the Landau-level quantization

We begin with the single-particle properties. Consider the following Hamiltonian of 2D two-component atomic gases with an artificial Rashba SO coupling defined as

$$H_0^{2D,R} = \frac{\vec{p}^2}{2M} + V_{\text{tp}}(\vec{r}) - \lambda_R(\sigma_x p_y - \sigma_y p_x), \quad (1)$$

where $\vec{p} = -i\hbar\vec{\nabla}$, M is the atomic mass, the pseudospin components \uparrow and \downarrow refer to two different internal atomic components, λ_R is the Rashba SO coupling strength with the unit of velocity, $V_{\text{tp}}(\vec{r}) = \frac{1}{2}M\omega^2 r^2$ is the external trapping potential and ω is the characteristic frequency of the trap. Another SO-coupled Hamiltonian will be considered in the 3D Weyl SO coupling defined as

$$H_0^{3D,W} = \frac{\vec{p}^2}{2M} + V_{\text{tp}}(\vec{r}) - \lambda_W \vec{\sigma} \cdot \vec{p}, \quad (2)$$

where λ_W is the SO coupling strength.

Even though we will mostly consider bosons for the Hamiltonians of equations (1) and (2), they possess a Kramer-type TR symmetry $T = i\sigma_y C$ satisfying $T^2 = -1$, where C is the complex conjugate operation. At the single-particle level, there is no difference between bosons and fermions. Both Hamiltonians are rotationally invariant but break the inversion symmetry. The 2D Hamiltonian (equation (1)) still possesses the reflection symmetry with respect to any vertical plane passing the centre of the trap. For the 3D Hamiltonian (equation (2)), no reflection symmetry exists.

These two typical types of SO interactions have received a lot of attention recently in the community of ultra-cold atoms due to their close connection to condensed matter physics. There have already been great experimental efforts on realizing the SO coupling through atom–light interactions [11–13, 15, 16, 60]. In fact, several proposals for experimental implementations of equations (1) and (2) have appeared in the literature [30, 34, 35, 54, 66].

In this section, we review the single-particle properties of equations (1) and (2) focusing on their topological properties. In section 2.1, their Berry phase structures in momentum space are presented. When the quadratic harmonic trap potential is imposed, the Landau-level-type quantization on the energy spectra appears with the TR symmetry as shown in section 2.2. This Landau-level quantization provides a clear way to understand novel phases of bosons after turning on interactions. In section 2.3, wavefunctions of the lowest Landau levels of equations (1) and (2) are explicitly provided. The topology of these Landau-level states are reviewed through edge and surface spectra in section 2.4.

2.1. Berry connections in momentum space

Both equations (1) and (2) possess non-trivial topology in momentum space. Let us begin with the 2D Rashba Hamiltonian (equation (1)) in the free space, i.e. $V_{\text{tp}} = 0$. Its lowest single-particle states in free space are not located at the origin of momentum space but around a ring with the radius $k_{\text{so}}^R = M\lambda_R/\hbar$. The spectra read

$$\epsilon_{\pm}(\vec{k}) = \frac{\hbar^2}{2M}(k \mp k_{\text{so}}^R)^2, \quad (3)$$

where \pm refer to the helicity eigenvalues of the operator $\vec{\sigma} \cdot (\hat{k} \times \hat{z})$. The corresponding two-component spin wavefunctions of plane-wave states $|\psi_{\vec{k}\pm}\rangle$ are solved as

$$|\psi_{\vec{k}\pm}\rangle = \frac{1}{\sqrt{2}} \begin{pmatrix} e^{-i\frac{\theta_{\vec{k}}}{2}} \\ \mp i e^{i\frac{\theta_{\vec{k}}}{2}} \end{pmatrix}, \quad (4)$$

where $\phi_{\vec{k}}$ is the azimuthal angle of \vec{k} in the xy -plane.

For bosons, the lower energy branch states with a fixed helicity are important. The Berry connection $\vec{A}(\vec{k})$ of positive helicity states $\psi_+(\vec{k})$ is defined as

$$\vec{A}(\vec{k}) = \langle \psi_{\vec{k}+} | i\vec{\nabla}_{\vec{k}} | \psi_{\vec{k}+} \rangle = \frac{1}{2k} \hat{e}_{\phi_{\vec{k}}}, \quad (5)$$

where $\hat{e}_{\phi_{\vec{k}}}$ is the unit vector along the azimuthal direction. The Berry curvature F_{ij} is defined as $F_{ij}(\vec{k}) = \partial_{k_i} A_j(\vec{k}) - \partial_{k_j} A_i(\vec{k})$. For a loop winding around the origin $\vec{k} = (0, 0)$, the Berry phase is

$$\oint d\vec{k} \cdot \vec{A}(\vec{k}) = \pi. \quad (6)$$

This is because a two-component spinor after rotating 360° does not return to itself but acquires a minus sign. Consequently, $F_{ij}(\vec{k})$ is zero everywhere except contributing a π -flux at the origin of momentum space.

Next we consider the 3D generalization of the Rashba SO coupling of the $\vec{\sigma} \cdot \vec{p}$ type, i.e. the Weyl coupling. Now in the free space without the trap, the lowest energy single-particle states are located around a sphere in momentum space with the radius also denoted as k_{so}^W with the value of $k_{\text{so}}^W = M\lambda_W/\hbar$, and the spectra are

$$\epsilon_{\pm}(\vec{k}) = \frac{\hbar^2}{2M}(k \mp k_{\text{so}}^W)^2, \quad (7)$$

where the subscripts \pm refer to the helicity eigenvalues of the operator $\vec{\sigma} \cdot \hat{k}$. The corresponding eigenstates are solved as

$$|\psi_{\vec{k}-}\rangle = \begin{pmatrix} -\sin \frac{\theta_{\vec{k}}}{2} \\ \cos \frac{\theta_{\vec{k}}}{2} e^{i\phi_{\vec{k}}} \end{pmatrix}, \quad |\psi_{\vec{k}+}\rangle = \begin{pmatrix} \cos \frac{\theta_{\vec{k}}}{2} \\ \sin \frac{\theta_{\vec{k}}}{2} e^{i\phi_{\vec{k}}} \end{pmatrix}, \quad (8)$$

where $\phi_{\vec{k}}$ and $\theta_{\vec{k}}$ are the azimuthal and polar angles of \vec{k} in the spherical coordinates. The Berry connection of the positive helicity states $\psi_{\vec{k},+}$ is

$$\vec{A}(\vec{k}) = \frac{1}{2} \tan \frac{\theta_{\vec{k}}}{2} \hat{e}_{\phi_{\vec{k}}}, \quad (9)$$

which is the vector potential for a unit magnetic monopole located at the origin of momentum space and $\hat{e}_{\phi_{\vec{k}}}$ is the azimuthal direction of \vec{k} . Defining $B_i = \frac{1}{2}\epsilon_{ijl}F_{jl}$, the corresponding Berry curvature is $\vec{B}(\vec{k}) = \frac{1}{2k^2}\hat{e}_{\vec{k}}$, where $\hat{e}_{\vec{k}}$ is the radial direction of \vec{k} .

2.2. Landau-level quantization in the harmonic trap from SO couplings

The SO couplings in equations (1) and (2) introduce an SO length scale even in the free space defined as $l_{\text{so}} = 1/k_{\text{so}}$. (Here and the following, we omit the superscripts of k_{so}^R and k_{so}^W without loss of generality.) The physical meaning of l_{so} is as follows: the low-energy states of equations (1) and

(2) are not of long-wave length as usual but featured with large magnitude of momentum depending on the SO coupling strength. l_{so} is the length scale of wavepackets that can be formed by using the low-energy states on the SO ring of equation (1) or the SO sphere of equation (2). On the other hand, in the typical experimental setup with ultra-cold quantum gases, a harmonic trap is used to confine atoms. The trapping potential $V(\vec{r}) = \frac{1}{2}m\omega^2 r^2$ introduces another length scale as $l_T = \sqrt{\hbar/(m\omega)}$ as the typical system size. The trap energy scale is $E_{tp} = \hbar\omega$.

It is useful to define a dimensionless parameter $\alpha = l_T/l_{so}$ to describe the relative strength of the SO coupling with respect to the trapping potential. Physically, α is the number of wavepackets which can be packed in the trap length. In the limit of large values of α , the trapping potential gives rise to Landau-level-type quantizations in both 2D and 3D SO coupling systems [27, 54, 80, 103].

The terminology of Landau levels in this section is generalized from the usual 2D magnetic case as *topological* single-particle level structures labelled by *angular momentum* quantum numbers with flat or nearly flat spectra. On open boundaries, Landau-level systems develop gapless surface or edge modes which are robust against disorders. We will see that the low-energy states of both equations (1) and (2) satisfy this criterion in the case $\alpha \gg 1$.

2.2.1. TR-invariant Landau levels from the 2D Rashba SO coupling. Let us briefly recall the usual 2D Landau level arising from the magnetic field. In the symmetric gauge with $\vec{A} = \frac{1}{2}B\hat{z} \times \vec{r}$, its Hamiltonian is simply equivalent to a 2D harmonic oscillator in a rotating frame as

$$H_{2D,LL} = \frac{(\vec{p} - \frac{e}{c}\vec{A})^2}{2M} = \frac{p^2}{2M} + \frac{1}{2}M\omega^2 r^2 - \omega L_z, \quad (10)$$

where $L_z = xp_y - yp_x$ and $\omega = \frac{|eB|}{Mc}$. Inside each Landau level, the spectra are degenerate with respect to the magnetic quantum number m . Non-trivial topology of Landau levels comes from the fact that m does not take all the integer values. For example, in the lowest Landau level, m starts from 0 and runs all the positive integer number. This chiral feature is a TR symmetry breaking effect due to the magnetic field.

Next let us consider the 2D Rashba SO coupling of equation (1) in the limit of $\alpha \gg 1$. The physics is most clearly illustrated in momentum representation. After being projected into the low-energy sector of the positive helicity states, the harmonic potential in momentum space becomes a Laplacian subjected to the Berry connection as

$$V_{tp}(\vec{\nabla}_{\vec{k}}) = \frac{M}{2}\omega^2(i\vec{\nabla}_{\vec{k}} - \vec{A}_{\vec{k}})^2, \quad (11)$$

where \vec{A} is given in equation (5) with a π -flux at the origin of the 2D k_x - k_y plane. In momentum space, the trapping potential quantizes the motion on the low-energy SO ring with radius k_{so} , and is mapped to a planar rotor problem. The moment of inertia in momentum space is $I_k = k_{so}^2 M_k$, where M_k is the mass in momentum space defined as $M_k = 1/(M\omega^2)$, and the angular dispersion of energy is $E_{agl}(j_z) = \hbar^2 j_z^2 / 2I_k = \frac{1}{2\alpha^2} j_z^2 E_{tp}$. Due to the π -flux phase at $\vec{k} = (0, 0)$, j_z is quantized to half-integer values. On the other hand, the radial component of the trapping

potential in momentum space is just the kinetic energy for the positive helicity states

$$H_K = \frac{1}{2}M_k\omega^2(k - k_{so})^2. \quad (12)$$

For states near the low-energy SO ring, the radial motion can be approximated as 1D harmonic oscillations, and the energy gap remains as $\hbar\omega$. Combining the radial and angular dispersions together, we arrive at

$$E_{n_r, j_z} \approx \left\{ n_r + \frac{j_z^2}{2\alpha^2} + \frac{1}{2}(1 - \alpha^2) \right\} E_{tp}, \quad (13)$$

where n_r is the radial quantum number, and $\frac{1}{2}(1 - \alpha^2)$ is the constant of zero-point energy.

The degeneracy over angular momentum quantum numbers is the main feature of the Landau-level quantization. For the Hamiltonian equation (1), although its spectra (equation (13)) are not exactly flat with respect to j_z , they are strongly suppressed at $\alpha \gg 1$; thus these low energy levels are viewed as Landau levels. The radial quantum number n_r serves as the Landau-level index and the gaps between Landau levels are roughly E_{tp} . For states in the n_r -th Landau level with $|j_z| \leq \sqrt{2}\alpha$, their energies remain lower than the bottom of the next Landau level; thus they can be viewed as gapped bulk states. Actually, the similarities of these SO-coupled states to Landau levels are more than just spectra flatness but their non-trivial topology, which will be explained in section 2.4.

2.2.2. 3D Landau levels from the Weyl SO coupling. The 3D Landau-level systems are not as well known as the 2D case of equation (10). Recently, a large progress has been made in generalizing equation (10) to 3D with exactly flat energy dispersions [44, 110]. In particular, they can be constructed with the full 3D rotation symmetry by coupling spin-1/2 fermions with the SU(2) gauge potential. The Hamiltonian is equivalent to a 3D harmonic oscillator plus the SO coupling as

$$H_{3D,LL} = \frac{p^2}{2M} + \frac{1}{2}M\omega^2 r^2 - \omega \vec{L} \cdot \vec{\sigma}. \quad (14)$$

Excitingly, the lowest Landau-level wavefunctions of equation (14) possess elegant analytic properties, satisfying the Cauchy–Riemann–Fueter condition of quaternionic analyticity. Just like the complex analyticity is essential for the construction of fractional quantum Hall–Laughlin states, the quaternionic analyticity is expected to play an important role in high-dimensional fractional topological states. These 3D Landau-level states preserve both TR and parity symmetry. The 3D Landau levels have also been generalized to the relativistic Dirac particles [111].

Now let us come back to the Hamiltonian of equation (2) with the 3D Weyl SO coupling and a trap potential. The parallel analysis to the 2D Rashba case applies. Again, in the limit of $\alpha \gg 1$, after the projection into the sector of the positive helicity states, the trap potential becomes $V_{tp}(\vec{\nabla}_{\vec{k}}) = \frac{1}{2}M(i\vec{\nabla}_{\vec{k}} - \vec{A}_{\vec{k}})^2$ and $\vec{A}_{\vec{k}}$ takes the form of a magnetic monopole one in equation (9). The problem is reduced to a spherical rotor problem in momentum space on the low-energy SO sphere with the radius k_{so} . The monopole structure of the Berry connection quantizes the total angular momentum j to

half-integer values. Similar to the 2D Rashba case, the low-energy spectra are approximated as

$$E_{n_r, j, j_z} \approx \left\{ n_r + \frac{j(j+1)}{2\alpha^2} + \frac{1}{2}(1-\alpha^2) \right\} E_{\text{tp}}. \quad (15)$$

Again the angular dispersion is strongly suppressed by the SO coupling at $\alpha \gg 1$. These spectra exhibit quasi-degeneracy over the 3D angular momentum good quantum numbers of j and j_z , and thus can be viewed as a 3D Landau-level quantization with TR symmetry. The length scale of these Landau-level states is also the SO length l_{so} . Topological properties of these Landau-level states will be studied in section 2.4.

2.3. Lowest Landau-level wavefunctions and parent Hamiltonians

The Landau-level energy spectra of equation (13) in 2D and equation (15) in 3D are not exactly flat but with weak dispersions over angular momentum quantum numbers. Nevertheless, parent Hamiltonians based on slight modification on equations (1) and (2) can be constructed. Their lowest Landau-level spectra are exactly flat and their wavefunctions can be solved analytically as shown in equations (17) and (19) below. These wavefunctions maintain the TR symmetry but break parity. In the limit of $\alpha \gg 1$ and for Landau-level states with angular momenta $|j_z| < \alpha$ in 2D or $j < \alpha$ in 3D, the lowest Landau-level wavefunctions of equations (1) and (2) are well approximated by these expressions.

For the 2D case, the parent Hamiltonian is just

$$H_0^{2D,P} = H_0^{2D,R} - \omega L_z \sigma_z, \quad (16)$$

where $L_z = xp_y - yp_x$ and the coefficient ω is the same as the trap frequency. As shown in [65], its lowest Landau-level wavefunctions are solved as

$$\psi_{2D, j_z}^{LLL}(r, \phi) = e^{-\frac{r^2}{2l_T^2}} \begin{pmatrix} e^{im\phi} J_m(k_{\text{so}}r) \\ -e^{i(m+1)\phi} J_{m+1}(k_{\text{so}}r) \end{pmatrix}, \quad (17)$$

where ϕ is the azimuthal angle, $j_z = m + \frac{1}{2}$, J_m is the m th-order Bessel function. The lowest Landau-level energy is exactly flat as $E^{LLL} = (1 - \frac{\alpha^2}{2})\hbar\omega$.

In the case of $\alpha \gg 1$ and for small values of $|j_z| \approx m < \alpha$, the decay of the wavefunctions (equation (17)) is controlled by the Bessel functions rather than the Gaussian factor. Their classic orbit radii scale as $\rho_{c, j_z} \approx ml_{\text{so}}$. Since L_z linearly depends on ρ_{c, j_z} , the effect of the $L_z \sigma_z$ term compared to that of the Rashba one is at the order of $\rho_{c, j_z} \omega / \lambda_R \approx m / \alpha^2 \ll 1$. Thus, equation (16) is simply reduced to equation (1) whose lowest Landau-level wavefunctions are well approximated by equation (17). In this case, the length scale of Landau-level states is determined by the SO length l_{so} instead of the trap length l_T . The reason is that these Landau levels are composed of plane-wave states with a fixed helicity on the low-energy Rashba ring. The confining trap further opens the gap at the order of $\hbar\omega$ between the SO-coupled Landau levels.

In contrast, in the opposite limit, i.e. $|j_z| \approx m \gg \alpha^2$, the $L_z \sigma_z$ term dominates and the Rashba term can be neglected. In this case, equation (16) is reduced to $p^2/2M + \frac{1}{2}M\omega^2 r^2 - \omega L_z \sigma_z$

with σ_z conserved. In each spin eigensector, it is just the usual Landau-level Hamiltonian in the symmetric gauge with opposite chiralities for spin up and down, respectively. Nevertheless, at $m \gg \alpha^2$, the approximation of the projection into the Rashba ring for equation (1) is not valid, and the eigenstates are no longer Landau levels. For the intermediate values of $\alpha < |j_z| < \alpha^2$, the physics is a crossover between the above two limits.

Following the same logic, the 3D parent Hamiltonian with exactly flat SO-coupled Landau levels is

$$H_0^{3D,P} = H_0^{3D,W} - \omega \vec{L} \cdot \vec{\sigma}, \quad (18)$$

where $\vec{L} = \vec{r} \times \vec{p}$ is the 3D orbital angular momentum, and the coefficient of the $\vec{L} \cdot \vec{\sigma}$ term is the same as the trap frequency. Again, as shown in [65], the lowest Landau-level wavefunctions of equation (18) are solved analytically as

$$\psi_{3D, j, j_z}^{LLL}(\vec{r}) = e^{-\frac{r^2}{2l_T^2}} \{ j_l(k_{\text{so}}r) Y_{+, j, l, j_z}(\Omega_r) + i j_{l+1}(k_{\text{so}}r) \times Y_{-, j, l+1, j_z}(\Omega_r) \}, \quad (19)$$

where j_l is the l th-order spherical Bessel function, Y_{\pm, j, l, j_z} are the SO-coupled spherical harmonics with total angular momentum quantum numbers $j = l \pm \frac{1}{2}$ and j_z , which are composed of the spherical harmonics Y_{lm} and spin-1/2 spinors. These lowest Landau-level states are degenerate over all the values of (j, j_z) with $E^{LLL} = (\frac{3}{2} - \frac{\alpha^2}{2})\hbar\omega$.

Following the same reasoning as in the 2D case, in the limit of $\alpha \gg 1$, we can divide the lowest Landau-level states of equation (19) into three regimes as $j < \alpha$, $j \gg \alpha^2$, and $\alpha < j < \alpha^2$, respectively. At $j < \alpha$, the classic orbit radius scales as $\rho_{c, j} / l_T \approx \frac{j}{\alpha}$, and thus $\vec{\sigma} \cdot \vec{L}$ compared with $\vec{\sigma} \cdot \vec{p}$ is a perturbation at the order of $j/\alpha^2 \ll 1$. In this regime, the lowest Landau-level wavefunctions of equation (2) are well approximated by equation (19). In contrast, in the regime of $j \gg \alpha^2$, $\vec{\sigma} \cdot \vec{L}$ dominates over $\vec{\sigma} \cdot \vec{p}$; thus the eigenstates of equations (18) and (2) are qualitatively different. In this case, equation (18) is reduced to the 3D Landau-level Hamiltonian (equation (14)).

2.4. The Z_2 -stability of helical edge and surface states

Non-trivial topology of the 2D Landau level manifests from the appearance of robust gapless edge states. The classic radius r_c of each Landau-level state expands as m increases. For example, in the lowest Landau level, $r_c = \sqrt{m} l_B$ where $l_B = \sqrt{\frac{\hbar c}{|eB|}}$ is the cyclotron radius. With an open boundary, as m becomes large enough, states are pushed to the boundary [112]. Unlike the flat bulk spectra, the edge spectra are dispersive, always increasing with m , and thus are chiral and robust against external perturbations. Each Landau level contributes one branch of chiral edge modes. If the system is filled with fermions, when chemical potential μ lies in the gap between Landau levels, the chiral edge states give rise to the quantized charge transport.

For Landau levels of the Rashba SO coupling in equation (1), a marked difference is that these states are TR invariant. The angular momentum j_z in equation (13) takes all the half-integer values as $j_z = \pm \frac{1}{2}, \pm \frac{3}{2}, \dots, \pm(m + \frac{1}{2}), \dots$, and thus these states are helical instead of chiral. Since the

system described by equation (1) does not possess translation symmetry, the usual method of calculating topological index based on lattice Bloch wave structures in Brillouin zones does not work [113–116].

Nevertheless, the non-trivial topology should exhibit on the robustness of edge states. The trap length l_T can be used as the sample size by imposing an open boundary condition at $r = l_T$. States with $|j_z| < \alpha$ are bulk states localized within the region of $r < l_T$. States with $|j_z| \sim \alpha$ are pushed to the boundary, whose spectra disperse to high energy rapidly. For a given energy E lying between Landau-level gaps, each Landau level with bulk energy below E contributes to a pair of degenerate edge modes $\psi_{\pm j_z}$ due to the TR symmetry. Nevertheless, these two edge modes are Kramer doublets under the TR transformation satisfying $T^2 = -1$. The celebrated Kane–Mele Z_2 argument for translational-invariant systems [113] can be generalized to these rotation-invariant systems by replacing linear momentum with the angular momentum. If a given energy cuts odd numbers of helical edge modes, then any TR-invariant perturbation cannot mix these modes to open a gap. Consequently, the topological nature of such a system is characterized by the Z_2 index.

When loading fermions in the system, and if the Fermi energy cuts the edge states, these helical edge states become active. The effective helical edge Hamiltonian can be constructed by imposing an open boundary at $r \approx l_T$. The effective helical edge Hamiltonian in the basis of j_z can be written as

$$H_{\text{edge}} = \sum_{j_z} \left(\frac{\hbar v_f}{l_T} |j_z| - \mu \right) \psi_{n_r, j_z}^\dagger \psi_{n_r, j_z}, \quad (20)$$

where μ is the chemical potential. If the edge is considered locally flat, then equation (20) can be rewritten in the plane-wave basis. Due to the reflection symmetry with respect to the plane perpendicular to the edge, the spin polarization for momentum p along the edge direction must lie in such a plane. Also, combining with the TR symmetry, we have

$$H_{\text{edge}} = v[(\vec{p} \times \hat{n}) \cdot \hat{z}](\sigma_z \sin \eta + (\vec{\sigma} \cdot \hat{n}) \cos \eta), \quad (21)$$

where \hat{n} is the local normal direction on the circular edge in the 2D plane, v is the linearized velocity of the edge modes around Fermi energy and η is a parameter angle depending on the details of the systems. There are the only terms allowed by rotation symmetry, TR symmetry and the vertical mirror symmetry in this system. Each edge channel is a branch of helical one-dimensional Dirac fermion modes.

Parallel analysis can be applied to the helical surface states of the 3D Hamiltonian equation (2). Again, due to the TR symmetry, surface states are helical instead of chiral. The topological class also belongs to Z_2 . If the surface is sufficiently large, and thus can be locally taken as flat, we can construct the surface Dirac Hamiltonian around the Fermi energy by using plane-wave basis basing on symmetry analysis. First, due to the local $SO(2)$ rotational symmetry around \hat{n} , the in-plane momenta p_x and p_y cannot couple to σ_z ; thus spin polarization for each in-plane momentum (p_x, p_y) has to lie in the xy -plane. Generally speaking, the spin polarization vector (s_x, s_y) forms an angle η with respect to (p_x, p_y) and such an angle

is determined by the details of the surface. Combining all the above information, we arrive at

$$H_{sfc} = v\{\sin \eta(\vec{p} \times \vec{\sigma}) \cdot \hat{n} + \cos \eta[\vec{p} \cdot \vec{\sigma} - (\vec{p} \cdot \hat{n})(\vec{\sigma} \cdot \hat{n})]\} \quad (22)$$

where \hat{n} is the local normal direction to the 2D surface.

3. Topological spin textures and the quaternionic phase defects in a harmonic trap

In this section, we review the unconventional BECs with interactions and SO couplings, including both Rashba and the 3D Weyl types, in the harmonic trap. The 2D Rashba case is presented in section 3.1. The linear dependence on the momentum of SO coupling invalidates the proof of the ‘no-node’ theorem. Consequently, a general feature of the SO-coupled BECs is the complex-valued condensate wavefunctions and the spontaneous TR symmetry breaking. For the Rashba case, the skyrmion-type spin textures and half-quantum vortex were predicted in the harmonic trap [27]. Furthermore, due to the Landau-level structures of single-particle states, rich patterns of spin textures have been extensively investigated in the literature [27, 45, 53]. A nice introduction of topological defects in the ultra-cold atom context can be found in [117–119].

Even more interesting physics shows in the 3D Weyl SO coupling, which will be reviewed in section 3.3. The non-trivial topology of the condensate wavefunction is most clearly expressed in the quaternionic representation [73, 111]. Quaternions are a natural extension of complex numbers as the first discovered non-commutative division algebra, which has been widely applied in quantum physics [120–122]. The condensation wavefunctions exhibit defects in the quaternionic phase space as the 3D skyrmions, and the corresponding spin density distributions are characterized by non-zero Hopf invariants.

3.1. Half-quantum vortices and spin texture skyrmions with the Rashba SO coupling

Let us consider a 3D two-component boson system with contact spin-independent interactions and with the Rashba SO coupling in the xy -plane. Since the Rashba SO coupling is 2D, interesting spin textures are only distributed in the xy -plane. For simplicity, the condensate is set uniform along the z -direction, and then the problem is reduced to a 2D Gross–Pitaevskii (GP) equation as

$$\left\{ -\frac{\hbar^2 \nabla^2}{2M} + i\hbar\lambda_R(\nabla_x \sigma_{y,\alpha\beta} - \nabla_y \sigma_{x,\alpha\beta}) + gn(r, \phi) + \frac{1}{2}M\omega^2 r^2 \right\} \psi_\beta(r, \phi) = E \psi_\alpha(r, \phi), \quad (23)$$

where ψ_α s with $\alpha = \uparrow, \downarrow$ are two-component condensate wavefunctions, $n(r, \phi)$ is the particle density and g describes the s-wave scattering interaction. The interaction energy scale is defined as $E_{\text{int}} = gN_0/(\pi l_T^2 L_z)$, where L_z is the system size along the z -axis, and the dimensionless interaction parameter is defined as $\beta = E_{\text{int}}/(\hbar\omega_T)$.

We start with the weak SO coupling, $\alpha \sim 1$, and with weak interactions. In this case, the energy of the single-particle ground state with $j_z = \pm \frac{1}{2}$ is well separated from other states. If interactions are not strong enough to mix the ground level with other levels, the condensate wavefunction remains the same symmetry structure carrying $j_z = \frac{1}{2}$, or, $-\frac{1}{2}$, thus bosons condense into one of the TR doublets,

$$\psi_{\frac{1}{2}}(r, \phi) = \begin{pmatrix} f(r) \\ g(r) e^{i\phi} \end{pmatrix}, \quad \psi_{-\frac{1}{2}}(r, \phi) = \begin{pmatrix} -g(r) e^{-i\phi} \\ f(r) \end{pmatrix}, \quad (24)$$

where $f(r)$ and $g(r)$ are real radial functions. In the non-interacting limit, $f(r) \approx J_0(k_{so}r) e^{-\frac{r^2}{4l_T^2}}$ and $g(r) \approx J_1(k_{so}r) e^{-\frac{r^2}{4l_T^2}}$ as shown in equation (17). Repulsive interactions expand the spatial distributions of $f(r)$ and $g(r)$, but the qualitative picture remains. Therefore, one spin component stays in the s-state and the other in the p-state. This is a half-quantum vortex configuration which spontaneously breaks the TR symmetry [27].

One possibility is that the condensate wavefunction may take linear superpositions of the Kramer doublet in equation (24). The superposition principle usually does not apply due to the nonlinearity of the GP equation. Nevertheless, if the interaction of the GP equation is spin-independent, then all the linear superpositions of the Kramer doublet in equation (24) are indeed degenerate. This is an accidental degeneracy at the mean-field level which is not protected. Quantum fluctuations remove this degeneracy as shown in the exact diagonalization calculation in [53] and select either one of $\psi_{\pm \frac{1}{2}}$. In other words, quantum fluctuations can induce a spin-dependent interaction beyond the mean-field level [27]. Certainly, we can also prepare the initial state with the average j_z per particle $\pm \frac{1}{2}$, say, by cooling down from the fully polarized spin up or down state; then $\psi_{\pm \frac{1}{2}}$ will be reached. On the other hand, if an additional spin-dependent interaction is introduced,

$$H'_{\text{int}} = g' \int d^3\vec{r} (n_{\uparrow}(r) - n_{\downarrow}(r))^2, \quad (25)$$

then even the mean-field level degeneracy is removed. In this case, as shown in [55], the condensate wavefunctions of $\psi_{\pm \frac{1}{2}}$ will also be selected.

The spin distribution of a condensate wavefunction is expressed as

$$\vec{S}(r, \phi) = \psi_{\alpha}^*(r, \phi) \vec{\sigma}_{\alpha\beta} \psi_{\beta}(r, \phi), \quad (26)$$

which is known as the first Hopf map. Without loss of generality, the condensate of $\psi_{\frac{1}{2}}$ is considered, and its $\vec{S}(\vec{r})$ is expressed as

$$\begin{aligned} S_x(r, \phi) &= \rho \sin 2\gamma(r) \cos \phi, & S_y(r, \phi) &= \rho \sin 2\gamma(r) \sin \phi, \\ S_z(r, \phi) &= \rho \cos 2\gamma(r), \end{aligned} \quad (27)$$

where $\rho(r) = \sqrt{|f(r)|^2 + |g(r)|^2}$, and the parameter angle $\gamma(r)$ is defined through

$$\cos \gamma(r) = \frac{f(r)}{\rho(r)}, \quad \sin \gamma(r) = \frac{g(r)}{\rho(r)}. \quad (28)$$

Since the Fourier components of $f(r)$ and $g(r)$ are located around the Rashba ring in momentum space, they oscillate

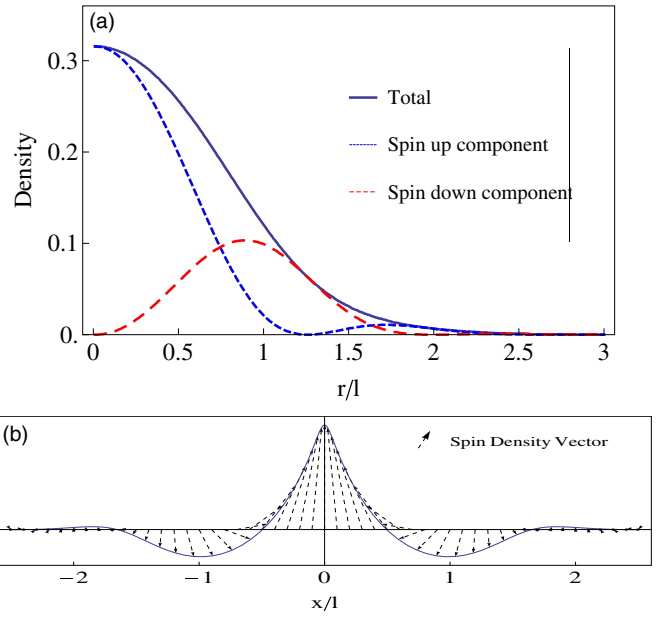


Figure 1. (a) The radial density distribution of spin up and down components, and the total density distribution in the unit of $N_0 = \int d^3\vec{r} \{ |\psi_{\uparrow}(\vec{r})|^2 + |\psi_{\downarrow}(\vec{r})|^2 \}$ at $\alpha = 2$ and $\beta = 5$. (b) The skyrmion-type spin texture configuration is plotted in the xz -plane. Reproduced with permission from [27]. © 2011 IOP Publishing.

along the radial direction with an approximated pitch value of k_{so} as shown in figure 1(a). Because $f(r)$ and $g(r)$ are of the s- and p-partial waves, respectively, they are with a relative phase shift of $\frac{\pi}{2}$. At $r = 0$, $f(r)$ is at maximum and $g(r)$ is 0. As r increases, roughly speaking, the zero points of $f(r)$ correspond to the extrema of $g(r)$ and vice versa; thus $\gamma(r)$ spirals as r increases. At the n th zero of $g(r)$ denoted r_n , $\gamma(r_n) = n\pi$ ($n \geq 0$ and we define $r_0 = 0$).

Consequently, \vec{S} spirals in the zx -plane along the x -axis as shown in figure 1(B). The entire distribution of \vec{S} can be obtained through a rotation around the z -axis. This is a skyrmion configuration which is a non-singular topological defect mapping from the real space R^2 to the spin orientation space of the S^2 sphere. If the coordinate space is a closed manifold S^2 , then this mapping is characterized by the integer-valued Pontryagin index $\pi_2(S^2) = Z$, or, the winding number. However, the coordinate space is the open R^2 , and $\rho(r)$ decays exponentially at large distance $r \gg l_T$; thus, rigorously speaking, the covering number is not well defined. Nevertheless, in each concentric circle $r_n < r < r_{n+1}$, $\gamma(r)$ varies from $n\pi$ to $(n+1)\pi$, which contributes to the winding number by 1. If we use the trap length scale l_T as the system size, the winding number is roughly at the order of α .

The radial oscillation of the spin density is in analogy to the Friedel oscillations in Fermi systems. Around an impurity in electronic systems, the screening charge distribution exhibits the radial oscillation on top of the enveloping exponential decay. The oscillation pitch is $2k_f$ reflecting the discontinuity of the Fermi distribution on the spherical Fermi surface. Different from the usual boson systems, the SO-coupled ones have a low-energy ring structure in momentum space in analogous to the Fermi surface; thus, in real space, spin density also oscillates in the presence of spatial inhomogeneity.

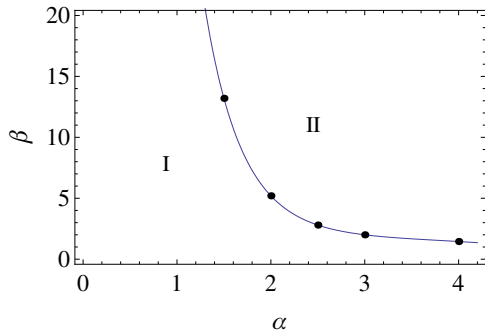


Figure 2. The phase boundary of β_c versus α between (I) the skyrmion condensates with $j_z = \pm \frac{1}{2}$ and (II) rotational symmetry breaking condensates. Reproduced with permission from [27]. © 2011 IOP Publishing.

In the regime of the intermediate SO coupling strength, the level spacing between single-particle states within the same Landau level is suppressed as shown in equation (13). In the case that interactions are strong enough to mix energy levels with different angular momenta in the same lowest Landau level but not among different Landau levels, condensates no longer keep rotation symmetry. The calculated phase boundary of the interaction strength β versus SO coupling strength α is plotted in figure 2. In this regime, the distributions are no longer concentric but split into multi-centres and finally form a triangular skyrmion lattice structure as calculated in [45, 53]. This 2D skyrmion lattice structure is a characteristic feature brought by the SO coupling.

3.2. Plane-wave type condensations with the Rashba SO coupling

If interactions are strong enough to mix states in different Landau levels, then the influence of the confining trap is negligible. The condensate configurations in the free space were calculated beyond the mean-field GP equation level in [27]. Bosons select the superposition of a pair of states with opposite momenta \vec{k} and $-\vec{k}$ on the low-energy Rashba ring to condense. The spin eigenstates of these two states are orthogonal; thus the condensate can avoid the positive exchange interactions. As is well known, avoiding exchange energy is the main driving force towards the BEC. For spin-independent interactions, the condensate wavefunctions exhibit degeneracy at the Hartree–Fock level regardless of the relative weight between these two plane-wave components. This is a phenomenon of ‘frustration’. Quantum zero-point energy from the Bogoliubov quasi-particle spectra selects an equal weight supposition through the ‘order-from-disorder’ mechanism. Such a condensate exhibits spin-spiral configuration.

Various literatures have also studied the case of spin-dependent interactions in which the Hartree–Fock theory is already enough to select either the spin-spiral state, or, a ferromagnetic condensate with a single plane-wave component [38, 39].

3.3. Quaternionic phase defects of the 3D Weyl SO coupling

Next, we review the condensates with the 3D Weyl SO coupling in the harmonic trap. The corresponding GP equation

is very similar to equation (23) of the Rashba case. Only slight modifications are needed by replacing the spatial dimension 2 with 3, and by replacing the Rashba term with $-i\hbar\lambda_W \vec{\nabla} \cdot \vec{\sigma}$. Amazingly, in this case condensate wavefunctions exhibit topological structures in the quaternionic representation [72].

3.3.1. The quaternionic representation. Just like a pair of real numbers form a complex number, the two-component spinor $\psi = (\psi_\uparrow, \psi_\downarrow)^T$ is mapped to a single quaternion following the rule

$$\xi = \xi_0 + \xi_1 i + \xi_2 j + \xi_3 k, \quad (29)$$

where $\xi_0 = \text{Re } \psi_\uparrow$, $\xi_1 = \text{Im } \psi_\downarrow$, $\xi_2 = -\text{Re } \psi_\downarrow$, $\xi_3 = \text{Im } \psi_\uparrow$. i, j, k are the imaginary units satisfying $i^2 = j^2 = k^2 = ijk = -1$, and the anti-commutation relation $ij = -ji = k$. Quaternion can also be expressed in the exponential form as

$$\xi = |\xi| e^{i\omega\gamma} = |\xi| (\cos \gamma + \omega \sin \gamma), \quad (30)$$

where $|\xi| = \sqrt{\xi_0^2 + |\vec{\xi}|^2}$ and $|\vec{\xi}|^2 = \xi_1^2 + \xi_2^2 + \xi_3^2$; ω is the unit imaginary unit defined as $\omega = (\xi_1 i + \xi_2 j + \xi_3 k)/|\vec{\xi}|$ which satisfies $\omega^2 = -1$; the argument angle γ is defined as $\cos \gamma = \xi_0/|\xi|$ and $\sin \gamma = |\vec{\xi}|/|\xi|$.

Similar to the complex phase $e^{i\phi}$ which spans a unit circle, the quaternionic phases $e^{i\omega\gamma}$ span a unit three-dimensional sphere S^3 . The spin orientations lie in the S^2 Bloch sphere. For a quaternionic wavefunction, its corresponding spin distribution is defined through the first Hopf map defined in equation (26) as a mapping $S^3 \rightarrow S^2$. Due to the homotopy groups [123, 124] $\pi_3(S^3) = \mathbb{Z}$ and $\pi_3(S^2) = \mathbb{Z}$, both quaternionic condensate wavefunctions and spin distributions can be non-trivial. The winding number of $S^3 \rightarrow S^3$ is the 3D skyrmion number, and that of the $S^3 \rightarrow S^2$ is the Hopf invariant, and both are integer-valued.

Let us apply the above analysis to the lowest single-particle level with $j_z = j = \frac{1}{2}$

$$\psi_{j=j_z=\frac{1}{2}}(r, \hat{\Omega}) = f(r) Y_{+\frac{1}{2}, 0, \frac{1}{2}}(\hat{\Omega}) + ig(r) Y_{-\frac{1}{2}, 1, \frac{1}{2}}(\hat{\Omega}), \quad (31)$$

where $Y_{+\frac{1}{2}, 0, \frac{1}{2}}(\hat{\Omega}) = (1, 0)^T$ and $Y_{-\frac{1}{2}, 1, \frac{1}{2}}(\hat{\Omega}) = (\cos \theta, \sin \theta e^{i\phi})^T$. As shown in equation (19), in the non-interacting limit, $f(r) \approx j_0(k_{so}r) e^{-\frac{r^2}{4l^2}}$ and $g(r) \approx j_1(k_{so}r) e^{-\frac{r^2}{4l^2}}$. The corresponding quaternionic expression is

$$\xi_{j=j_z=\frac{1}{2}}(r, \hat{\Omega}) = \rho(r) e^{\omega(\hat{\Omega})\gamma(r)}, \quad (32)$$

where $\rho(r)$ and $\gamma(r)$ are defined in the same way as the 2D case in equation (27); the imaginary unit,

$$\omega(\hat{\Omega}) = \sin \theta \cos \phi i + \sin \theta \sin \phi j + \cos \theta k, \quad (33)$$

is along the direction of $\hat{\Omega}$.

3.3.2. The skyrmion-type 3D quaternionic phase defects. The analysis on the topology of the Weyl condensates can be performed in parallel to the above 2D Rashba case. Again in the case of the weak SO coupling, interactions only expand the spatial distribution of $f(r)$ and $g(r)$ in equation (31) from their non-interacting forms. The radial wavefunctions $f(r)$ and $g(r)$ follow the same oscillating patterns as those in the Rashba

case, so does the parameter angle $\gamma(r)$ which starts from 0 at the origin and reaches $n\pi$ at the n th zero of $f(r_n) = 0$. For the quaternionic phase $e^{\omega(\hat{\Omega})\gamma(r)}$, its imaginary unit $\omega(\hat{\Omega})$ is of one-to-one correspondence to every direction in 3D; thus it exhibits a non-trivial mapping from the 3D coordinate space R^3 to S^3 , which is known as a 3D skyrmion configuration.

For a closed 3-manifold, the Pontryagin index of winding number is $\pi_3(S^3) = Z$, i.e. integer. Again here the real space is open. In each concentric spherical shell with $r_n < r < r_{n+1}$ whose thickness is at the scale of l_{so} , $\gamma(r)$ spirals from $n\pi$ to $(n+1)\pi$; thus this shell contributes 1 to the winding number from real space to the quaternionic phase manifold. If the system size is truncated at the trap length l_T , again the winding number is approximately α . In comparison, in the 2D Rashba case reviewed in section 3.1, $\vec{S}(\vec{r})$ exhibits the 2D skyrmion configuration [27, 45, 53], but condensation wavefunctions have no well-defined topology due to the fact that $\pi_2(S^3) = 0$.

A comparison can be made with the $U(1)$ vortex in the single-component BEC. In 2D, it is a topological defect with a singular core. Moving around the circle enclosing the core, the phase winds from 0 to 2π , and thus the winding number is 1. The above 3D skyrmion phase defect is a natural generalization to the two-component case whose phase space is S^3 in the quaternionic representation and is isomorphic to the $SU(2)$ group manifold. These 3D skyrmions are non-singular defects similar to a 1D ring of rotating BEC which carries a non-zero phase winding number but the vortex core lies outside the ring.

3.3.3. Spin textures with non-zero Hopf invariants. The non-trivial topology of the condensate wavefunctions leads to a topologically non-trivial distribution of spin density $\vec{S}(\vec{r})$. The first Hopf map defined in equation (26) becomes very elegant in the quaternionic representation as

$$S_x i + S_y j + S_z k = \frac{1}{2} \bar{\xi} k \xi, \quad (34)$$

where $\bar{\xi} = \xi_0 - \xi_1 i - \xi_2 j - \xi_3 k$ is the quaternionic conjugate of ξ . For the condensate wavefunction (equation (32)), $\vec{S}(\vec{r})$ is calculated as

$$\begin{aligned} \begin{bmatrix} S_x(\vec{r}) \\ S_y(\vec{r}) \end{bmatrix} &= g(r) \sin \theta \begin{bmatrix} \cos \phi & -\sin \phi \\ \sin \phi & \cos \phi \end{bmatrix} \begin{bmatrix} g(r) \cos \theta \\ f(r) \end{bmatrix}, \\ S_z(\vec{r}) &= f^2(r) + g^2(r) \cos 2\theta, \end{aligned} \quad (35)$$

which exhibits a perfect axial symmetry around the z -axis. $\vec{S}(\vec{r})$ is plotted in figure 3 at different cross sections. In the xy -plane, it exhibits a 2D skyrmion pattern, whose in-plane components are along the tangential direction. As the horizontal cross-section shifted along the z -axis, $\vec{S}(\vec{r})$ remains the 2D skyrmion-like, but its in-plane components are twisted around the z -axis. According to the sign of the interception z_0 , the twist is clockwise or anti-clockwise, respectively. This 3D distribution pattern of $\vec{S}(\vec{r})$ is characterized by an integer-valued Hopf invariant characterized by $\pi_3(S^2) = Z$.

As SO coupling strength increases, condensates break rotational symmetry by mixing different states with different values of j in the lowest Landau level. Even at the intermediate level of SO coupling, rich patterns appear. The quaternionic phase defects and the corresponding spin textures split into a multi-centred pattern as plotted in figure 4 for different

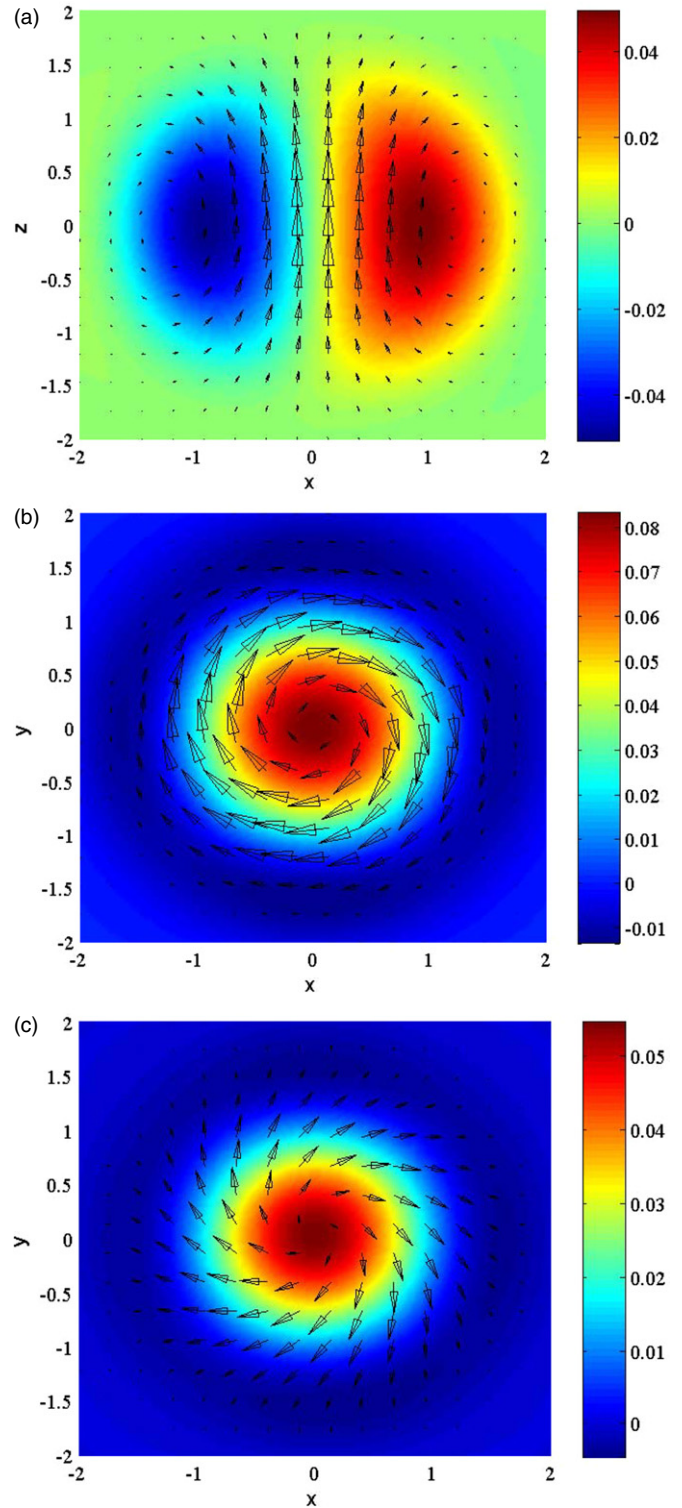


Figure 3. The distribution of $\vec{S}(\vec{r})$ in (a) the xz -plane and in the horizontal planes with (b) $z = 0$ and (c) $z/l_T = \frac{1}{2}$ with $\alpha = 1.5$, $c = 1$ and $\beta = 30$. The colour scale shows the magnitude of out-plane component S_y in (a) and S_z in (b) and (c). The 3D distribution of $\vec{S}(\vec{r})$ is topologically non-trivial with a non-zero Hopf invariant. The length unit in all the figures is l_T . Reproduced with permission from [72].

horizontal cross-sections. In the xy -plane, \vec{S} exhibits a multiple skyrmion configuration as shown in the combined pattern of the in-plane and z -components. Again this pattern is twisted

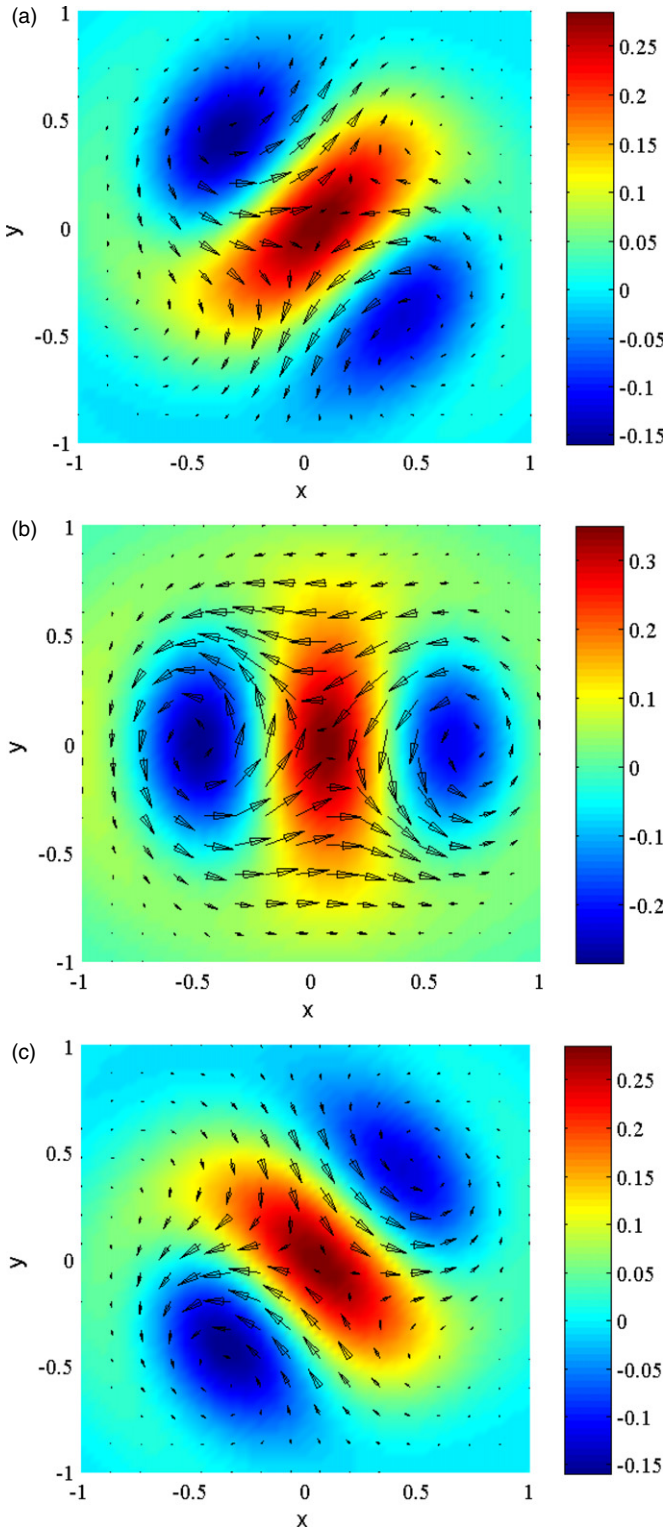


Figure 4. The distribution of $\vec{S}(\vec{r})$ in horizontal cross-sections with (a) $z/l_T = -0.5$, (b) $z/l_T = 0$, (c) $z/l_T = 0.5$, respectively. The colour scale shows the value of S_z , and parameter values are $\alpha = 4$, $\beta = 2$, and $c = 1$.

by rotating around the z -axis as the interception value z varies. Thus the whole 3D configuration also possesses a non-trivial Hopf invariant.

In particular, in the case of $\alpha \gg 1$, it is expected that a 3D lattice structure of topological defects may be formed, which

is a generalization of the 2D skyrmion lattice configuration in [53] into 3D. Again, if interaction is very strong to mix states in different Landau levels, the condensate will become plane-wave-like or superpositions of SO-coupled plane waves [72].

4. Vortex configurations of SO-coupled BECs in a rotating trap

Next, we review the vortex configurations of SO-coupled unconventional BECs in rotating traps. From a more general framework, the above-considered SO coupling can be viewed as particles subject to non-Abelian gauge fields. On the other hand, the Coriolis force from rotation behaves as an effective Abelian vector potential. Therefore, in a rotating trap, the atom-laser coupling provides an elegant way to study the effects of these two different effective gauge fields. We only consider the rotating systems with the Rashba SO coupling.

4.1. Hamiltonians of SO-coupled bosons in a rotating trap

Ultracold atoms in a rotating trap share similar physics of electrons subject to magnetic fields due to the similarity between Lorentz and Coriolis forces. Depending on the experimental implementations of rotation, Hamiltonians can be of different types [81, 82, 85]. As pointed out in [81], because the current experiment setup breaks rotation symmetry, rotating SO-coupled BECs are time-dependent in the rotating frame, which is a considerably more complicated problem than the usual rotating BECs. Nevertheless, below we only consider the situation of the isotropic Rashba SO coupling, such that it, in principle, can be implemented as a time-independent problem in the rotating frame.

The effect of rotation should be described by the standard minimal substitution method as presented in [85]. The non-interacting part of the Hamiltonian is

$$H_0 = \int d^3\vec{r} \psi_\mu^\dagger(\vec{r}) \left[\frac{1}{2M} (-i\hbar\vec{\nabla} + M\lambda\hat{z} \times \vec{\sigma} - \vec{A})^2 - \mu + V_{tr}(\vec{r}) - \frac{1}{2}M\Omega_z^2(x^2 + y^2) \right] \psi_\nu(\vec{r}), \quad (36)$$

where $\vec{A} = m\Omega_z\vec{r} \times \hat{z}$, and the last term is the centrifugal potential due to rotation.

Note that due to the presence of the SO coupling, we should carefully distinguish the difference between mechanical and canonical angular momenta. The mechanical one should be defined according to the minimal substitution as

$$L^{\text{mech}} = L_z + M\lambda(x\sigma_x + y\sigma_y), \quad (37)$$

where L_z is the usual canonical angular momentum. Expanding equation (36), it is equivalent to equation (1) plus the term of angular velocity Ω_z coupling to L^{mech} as

$$H_{\text{rot}} = -\Omega_z \int d^3\vec{r} \psi_\mu^\dagger(\vec{r}) [L^{\text{mech}}]_{\mu\nu} \psi_\nu(\vec{r}). \quad (38)$$

Thus in the rotating frame, the effect of Ω_z is not only just $\Omega_z L_z$ as usual, but also an extra effective radial Zeeman term as

$$\vec{B}_R(\vec{r}) = \Omega_z M\lambda\vec{r}. \quad (39)$$

Such a term is often missed in the literature. As will be shown below, it affects the ground state vortex configurations significantly and thus should not be overlooked.

To make the model more adjustable, an external spatially dependent Zeeman field $\vec{B}_{\text{ex}} = B\vec{r}$ is intentionally introduced as

$$H_B = -B \int d^3r \psi_\mu^\dagger(\vec{r})(x\sigma_x + y\sigma_y)_{\mu\nu} \psi_\nu(\vec{r}), \quad (40)$$

which shares the same form as equation (39). Experimentally, such a Zeeman field can be generated through coupling two spin components using two standing waves in the x - and y -directions with a phase difference of $\pi/2$. The corresponding Rabi coupling is

$$-\Omega \{ \sin(k_L x) + i \sin(k_L y) \} \psi_\downarrow^\dagger(\vec{r}) \psi_\uparrow(\vec{r}) + \text{h.c.} \quad (41)$$

In the region of $|x|, |y| \ll 2\pi/k_L$, it reduces to the desired form of equation (40) with $B = \Omega/k_L$. Such a term compensates the non-canonical part of the mechanical momentum in H_{rot} , which renders the model adjustability in a wider range.

4.2. SO-coupled bosons in rotating traps

Now we turn on interactions and obtain the ground state condensate numerically by solving the SO-coupled GP equations which have been reduced into the dimensionless form as

$$\begin{aligned} \mu \tilde{\psi}_\uparrow &= \hat{T}_\uparrow \tilde{\psi}_\uparrow + \beta (|\tilde{\psi}_\uparrow|^2 + |\tilde{\psi}_\downarrow|^2) \tilde{\psi}_\uparrow, \\ \mu \tilde{\psi}_\downarrow &= \hat{T}_\downarrow \tilde{\psi}_\downarrow + \beta (|\tilde{\psi}_\downarrow|^2 + |\tilde{\psi}_\uparrow|^2) \tilde{\psi}_\downarrow, \end{aligned} \quad (42)$$

where $(\tilde{\psi}_\uparrow, \tilde{\psi}_\downarrow)$ are normalized according to the condition $\int d\vec{r}^2 (|\tilde{\psi}_\uparrow|^2 + |\tilde{\psi}_\downarrow|^2) = 1$. \hat{T} is defined as

$$\begin{aligned} \hat{T} &= -\frac{1}{2} l_T^2 (\partial_x^2 + \partial_y^2) + \alpha l_T (-i\partial_y \sigma_x + i\partial_x \sigma_y) \\ &\quad + \frac{1}{2 l_T^2} (x^2 + y^2) - \frac{\rho}{l_T} (-ix\partial_y + iy\partial_x) \\ &\quad - \alpha \frac{\kappa}{l_T} (x\sigma_x + y\sigma_y), \end{aligned} \quad (43)$$

where $\rho = \Omega_z/\omega$, $\kappa = \gamma + \rho$ and $\gamma = B/(M\omega\lambda)$ is defined for the extra radial Zeeman field in equation (40).

4.2.1. The skyrmion lattice structure in the weak SO coupling. Rich structures of vortex lattices appear in the case of the weak SO coupling. In figure 5, the SO parameter is taken as $\alpha = 0.5$. Both the density and phase patterns for $\psi_\uparrow(r)$ and $\psi_\downarrow(r)$ are depicted. Let us first consider the case of pure rotation of $B = 0$ as shown in figure 5(d), i.e. $\gamma = 0$. For $\psi_\uparrow(r)$, its density distribution exhibits several disconnected peaks. By contrast, the usual vortex lattices show disconnected low density vortex cores. The phase distribution $\psi_\uparrow(r)$ exhibits singular points around which phases wind 2π . These singular points are squeezed out to the low-density region near the edge. For $\psi_\downarrow(r)$, its vortex cores are pinned by peaks of the density of $\psi_\uparrow(r)$. Combining the distributions of $\psi_\uparrow(r)$ and $\psi_\downarrow(r)$ together, the condensate exhibits a skyrmion lattice configuration with the spin distribution $\langle \vec{S} \rangle$, as shown in figure 6.

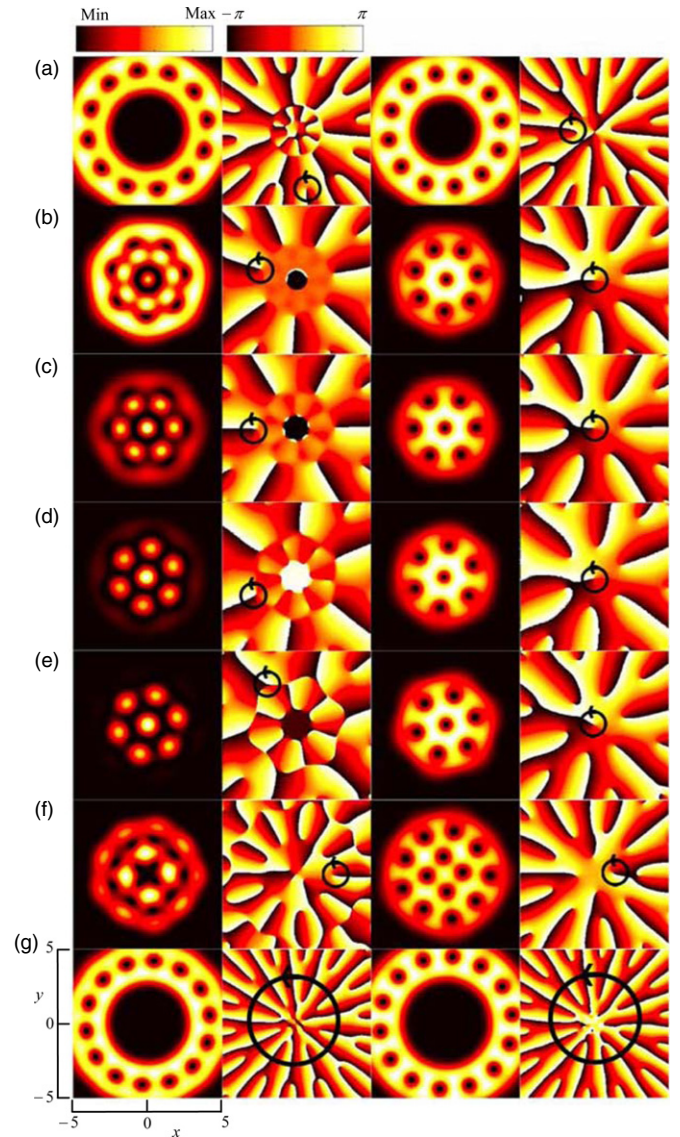


Figure 5. From left to right: the density and phase profiles of $\psi_\uparrow(r)$ and $\psi_\downarrow(r)$ with parameter values of $\alpha = 0.5$, $\beta = 10$, $\rho = 0.97$. From (a) to (g), γ is taken as 0.5, 0.25, 0.1, 0.0, -0.1, -0.3 and -0.5, respectively. At small values of $|\gamma|$ in (c)–(e), a skyrmion lattice is formed near the trap centre. By increasing the magnitude of $|\gamma|$ ((b) and (f)), the skyrmion lattice evolves to the normal vortex lattice. For the large value of $|\gamma| = 0.5$ ((a) and (g)), the condensates show a lattice configuration around a ring. The black circle with an arrow indicates the direction of the circulation around the vortex core. The unit of length for the figures is l_T . Reproduced with permission from [85]. © 2011 American Physical Society.

Turning on the external Zeeman field \vec{B}_{ex} of equation (40) changes the lattice configuration. If $\vec{B}_{\text{ex}} \parallel \vec{B}_R$, the parameter $\gamma > 0$; otherwise $\gamma < 0$. For both $\gamma > 0$ and $\gamma < 0$, if $|\gamma|$ is small, then the skyrmion lattice structures remain as depicted in figures 5(b), (c), (e) and (f). Increasing $|\gamma|$ further, the condensates of both spin components are pushed outwards, and distribute around a ring with a giant vortex core, as shown in figures 5(a) and (g). This ring is the location of potential minima shifted from the trap centre by the H_B term. In all cases in figures 5(a)–(g), the difference of vortex numbers between the spin-up and spin-down components is 1. This is a characteristic feature brought by the Rashba SO coupling.

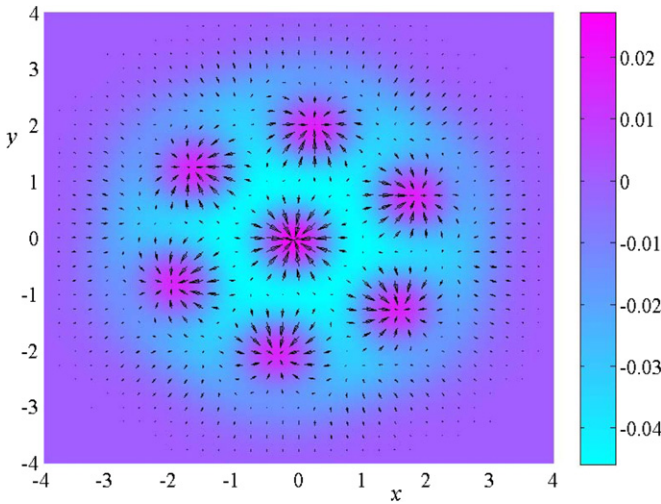


Figure 6. The spin density distribution of the condensate of figure 5(d). The projection of $\langle \vec{\sigma} \rangle$ in the xy -plane is shown as black vectors. A colour map is used to illustrate the $\langle \sigma_z \rangle$ component. The unit of length for the figure is l_T . Reproduced with permission from [85]. © 2011 American Physical Society.

4.2.2. The domain wall structure in the strong SO coupling. As discussed in section 3.2, in the case of the strong SO coupling, if interactions are also strong, condensates are nearly superpositions of SO-coupled plane-wave states subject to the trap boundary condition. We consider the effect of rotation in this case. Limited by the numeric convergence, only a small rotation angular velocity is considered. The term of the external Zeeman field \vec{B}_{ex} of equation (40) is also applied, which enriches the structures of the condensates as shown in figure 7.

The characteristic feature is that the condensate around the trap centre is broken into several domains. Inside each domain, the condensate is approximated as a plane-wave state. Wavevectors are arranged such that the local spin polarizations are parallel to \vec{B}_{ex} in order to minimize the Zeeman energy. At small values of $|\gamma|$ as shown in figures 7(c) and (d), a line of vortices appear at the boundary to separate two adjacent domains. Depending on the direction of \vec{B}_{ex} , the wavevectors inside domains can be clockwise or counterclockwise. For instance, when $\gamma > 0$, a clockwise configuration of these local wavevectors is selected in the condensate. On further increasing $|\gamma|$, different domains connect together to form a giant vortex as shown in figures 7(a), (g) and (h). Both spin components overlap with each other, and distribute around a ring with the radius of $\alpha|\gamma|l_T$. The spin textures lie along the radial direction to minimize the magnetic energy.

5. Strongly correlated phases of SO-coupled bosons

Ultracold atoms with the SO coupling provide us a unique opportunity of manipulating strongly correlated topological states in a highly controllable way. With current technology, it becomes experimentally feasible to implement effective magnetic fields in atomic systems through laser-atom interactions [11, 128, 129]. Since these systems share similar Hamiltonians with the solid state quantum Hall physics, this enables us to investigate various strongly correlated physics in

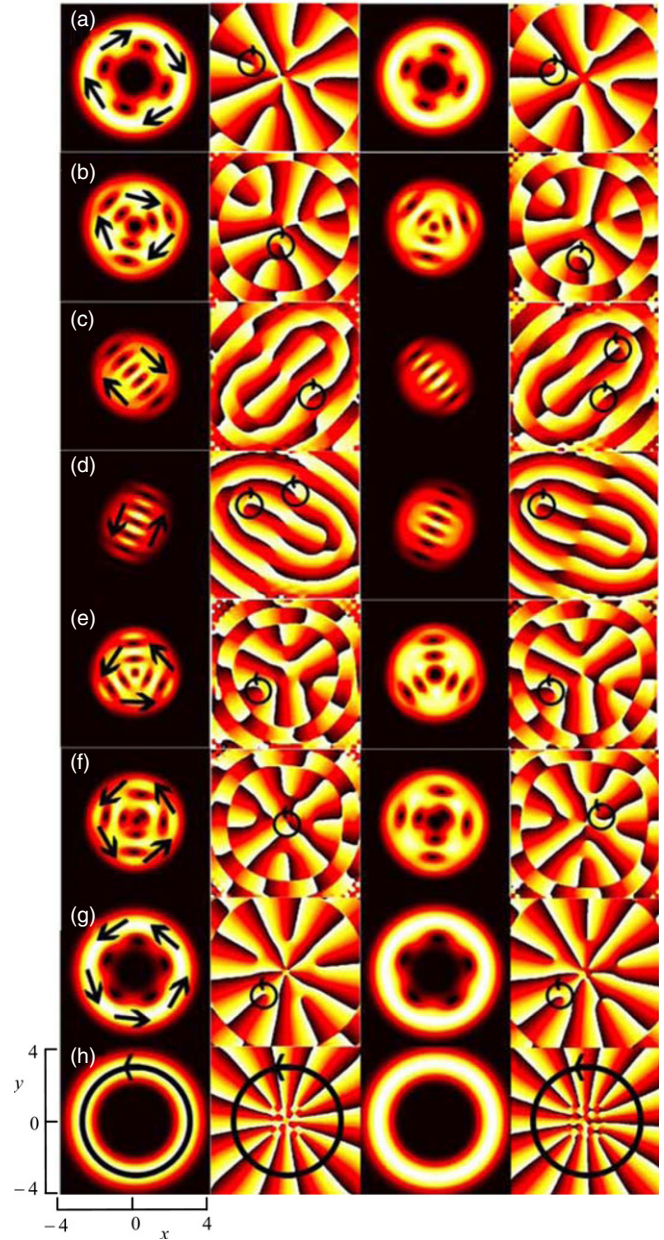


Figure 7. From left to right: the density and phase profiles of $\psi_{\uparrow}(r)$ and $\psi_{\downarrow}(r)$ with parameter values of $\alpha = 4$, $\beta = 20$, $c = 1$ and $\rho = 0.1$. From (a) to (h), γ is taken as 0.5, 0.3, 0.1, -0.05 , -0.25 , -0.35 , -0.6 and -0.7 , respectively. The black arrow in each domain represents the local wavevector direction of the corresponding plane-wave state, which shows a clockwise or counter-clockwise configuration depending on the sign of γ . For sufficiently large values of $|\gamma|$, condensates distribute around a ring in space forming a giant vortex. The colour scales for the density and phase distributions are the same as that in figure 5. The black circle with an arrow indicates the direction of the circulation around the vortex core. The unit of length for the figures is l_T . Reproduced with permission from [85]. © 2011 American Physical Society.

the presence of strong interactions. In addition, the realization of SO coupling effects using atoms also paves the way for searching for novel phases with non-trivial topology beyond traditional electronic systems.

Considerable progress has also been made along this direction. For instance, in [86], Ramachandran *et al*

have calculated the few-body physics using the exact diagonalization scheme for 2D SO-coupled bosons confined in a harmonic trap. A strongly correlated ground state with non-trivial topology has been reported at strong interaction strengths. For pseudospin-1/2 bosons subject to effective magnetic fields perpendicular to the 2D plane with the periodic boundary condition, it has been shown in [41, 42] that a Rashba-like SO coupling favours different quantum Hall phases depending on the coupling strengths. When the lowest Landau-level approximation is valid for large Landau-level gaps, the spin-polarized fractional quantum Hall states are formed for short-range interactions with Abelian excitations. Around some particular degenerate points where two Landau levels have the same energy, the ground states of the system are defined as deformed Halperin states. The non-Abelian nature of their anyonic excitations is crucial for the realization of topological quantum computations [125, 126]. Numerical investigations of these strongly correlated states at different filling factors have also been addressed recently [87–90]. We note that due to the rapid development of the area, many novel topological quantum phases are expected to be found within SO-coupled atomic systems.

6. Magnetic phases of SO-coupled bosons in optical lattices

It is natural to further consider the SO coupling effect in optical lattices, in particular in the Mott-insulating states [91–95]. Due to the SO coupling, hopping amplitudes are spin-dependent whose values vary non-monotonically with increasing SO coupling strength. The spin-dependent hopping leads to the Dzyaloshinsky–Moriya (DM)-type spin exchange models in the Mott-insulating states, which results in rich spin ordering patterns.

Due to the scope and limitation of this paper, we do not cover the synthetic gauge fields on optical lattices, which needless to say is an important research topic. In [29], Jaksch and Zoller proposed a theoretical scheme to generate artificial magnetic fields on lattices. Later on, this method has been generalized to generate non-Abelian $SU(N)$ gauge fields. The single-particle spectra exhibit a generalized Hofstadter butterfly structure [31]. In addition, there has been a large experimental progress in the synthetic effective magnetic fields in 2D lattices [127–129]. More details about creating artificial gauge fields with neutral atoms and some recent developments can be found in [35–37].

6.1. Tight-binding approximation and band parameters

The tight-binding model in the square optical lattice will be derived below for two-component bosons with the synthetic SO coupling. The single-particle Hamiltonian in the continuum is defined as in equation (1) by replacing the trapping potential with the periodic lattice potential as

$$V(x, y) = -V_0[\cos^2 k_0 x + \cos^2 k_0 y], \quad (44)$$

where $k_0 = 2\pi/\lambda_0$ and the lattice constant $a = \lambda_0/2$. The recoil energy is defined as $E_r = \hbar^2 k_0^2/(2M)$. For later

convenience, the relative strength of the SO coupling is quantified by the dimensionless parameter k_{so}/k_0 with $k_{so} = M\lambda_R$.

A tight binding Hamiltonian for the lowest orbital band with the SO coupling can be written as [91]

$$H = - \sum_{\langle ij \rangle, \sigma} t_{ij; \sigma \sigma'} [b_{i, \sigma}^\dagger b_{j, \sigma'} + \text{h.c.}] + \sum_i \left[\frac{U}{2} n_i^2 - \mu n_i \right], \quad (45)$$

where only the nearest-neighbour hoppings are included. $t_{ij; \sigma \sigma'}$ can be decomposed into spin-independent and spin-dependent components based on the following symmetry analysis:

$$t_{ij; \sigma \sigma'} = t + i\vec{\lambda}_{ij} \cdot \vec{\sigma}. \quad (46)$$

The coefficient of spin-dependent hopping is purely imaginary as a requirement of the TR symmetry. The optical lattice with the Rashba SO coupling possesses the reflection symmetry with respect to the vertical plane passing bonds along the x - and y -directions. These reflection symmetries require that $\vec{\lambda}_{i, i+\hat{e}_x} \parallel \hat{e}_y$ and $\vec{\lambda}_{i, i+\hat{e}_y} \parallel -\hat{e}_x$. The four-fold rotation symmetry requires that $\vec{\lambda}_{i, i+\hat{e}_x} \cdot \hat{e}_y = -\vec{\lambda}_{i, i+\hat{e}_y} \cdot \hat{e}_x$. All these symmetry properties together constraint the spin-dependent hopping up to a single parameter λ as

$$\lambda_{i, i+\hat{e}_x} = \lambda \hat{e}_y, \quad \lambda_{i, i+\hat{e}_y} = -\lambda \hat{e}_x. \quad (47)$$

The band structure parameters t and λ are related to the overlap integrals of the onsite SO-coupled Wannier functions in neighbouring sites. In the case of a deep lattice, each site can be approximated by a local harmonic potential. The lowest energy Wannier states $\psi_{j_z = \pm \frac{1}{2}}$ are a pair of Kramer doublets as presented in equation (24). The radial wavefunctions of the Wannier states $f(r)$ and $g(r)$ exhibit the Friedel-type oscillations as explained in section 3.1. Thus, naturally t and λ should also exhibit such oscillations with increasing the SO coupling parameter k_{so}/k_0 . This feature is numerically confirmed using the following method. The tight-binding band spectra can be calculated easily as

$$E_{\pm}(\vec{k}) = \varepsilon(\vec{k}) \pm 2\lambda \sqrt{\sin^2 k_x + \sin^2 k_y}, \quad (48)$$

where $\varepsilon(\vec{k}) = -2t(\cos k_x + \cos k_y)$. On the other hand, the band spectra can be calculated directly from the continuum model with the lattice potential (equation (44)) by using the basis of plane waves. By fitting these spectra using equation (48), the values of t and λ are obtained and are plotted in figure 8. Both t and λ oscillate with increasing k_{so}/k_0 , and the amplitudes of their overall envelopes decay. For the spectra of equation (48), the square lattice breaks the rotational symmetry down into the four-fold one; thus, the degeneracy of the Rashba ring is lifted. The lower band has the four-fold degenerate minima located at $\vec{Q} = (\pm k, \pm k)$ with

$$k = \tan^{-1} \frac{1}{\sqrt{2}} \frac{\lambda}{t}. \quad (49)$$

It should be pointed out that these lowest local Wannier states are the eigenstates of the on-site total angular momentum with $j_z = \pm \frac{1}{2}$. Therefore, the eigenbases defined by $(b_{i\uparrow}, b_{i\downarrow})^T$ should be those of j_z and not σ_z . In the case of the strong SO coupling $k_{so} \geq k_0$, the angular momenta of these Wannier states nearly come from the orbital angular momentum, while their spin moments are nearly averaged to zero.

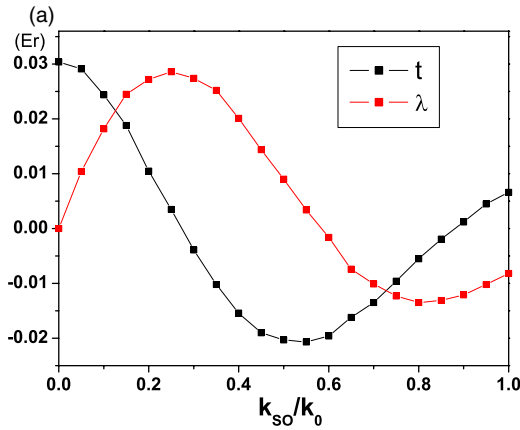


Figure 8. The dependence of the spin-independent hopping integral t and the spin-dependent one λ versus the SO coupling strength k_{so}/k_0 . The optical potential depth is $V_0 = 8E_r$. Reproduced with permission from [91]. © 2012 American Physical Society.

If in the limit of very strong SO coupling such that $k_{\text{so}} \gg k_0$, Landau-level quantization effects appear within each site. Many states with different values of j_z are nearly degenerate as presented in section 2.2. In this case, a single band model equation (45) fails even in the case of the deep lattice. It is justified only in the case when $k_{\text{so}}/k \leq 1$, in which the lowest Wannier states are separated from others.

6.2. Magnetic properties in the Mott-insulating state

We consider the spin physics in the Mott-insulating phase of equation (45). In the simplest case, there is one particle per site with a two-fold degenerate Kramer doublet. The low-energy superexchange Hamiltonian can be constructed using the Schrieffer–Wolf transformation, which shows the DM type exchange due to the SO coupling [130, 131] as

$$H_{\text{eff}} = \sum_i H_{i,i+\hat{e}_x} + H_{i,i+\hat{e}_y} \quad (50)$$

and

$$H_{i,i+\hat{e}_\mu} = -J_1 \vec{S}_i \cdot \vec{S}_{i+\hat{e}_\mu} - J_{12} \vec{d}_{i,i+\hat{e}_\mu} \cdot (\vec{S}_i \times \vec{S}_{i+\hat{e}_\mu}) + J_2 [\vec{S}_i \cdot \vec{S}_{i+\hat{e}_\mu} - 2(\vec{S}_i \cdot \vec{d}_{i,i+\hat{e}_\mu})(\vec{S}_{i+\hat{e}_\mu} \cdot \vec{d}_{i,i+\hat{e}_\mu})], \quad (51)$$

where \hat{e}_μ ($\mu = x, y$) are the unit vectors along the x - and y -directions, respectively; $J_1 = 4t^2/U$, $J_{12} = 4t\lambda/U$ and $J_2 = 4\lambda^2/U$. The DM vectors are defined as $\vec{d}_{i,i+\hat{e}_x} = \hat{e}_y$ and $\vec{d}_{i,i+\hat{e}_y} = -\hat{e}_x$ which are perpendicular to each other. This is similar to the case of the high T_c cuprate superconductors such as $\text{YBa}_2\text{Cu}_3\text{O}_6$ [132, 133]. Consequently, these DM vectors in equation (51) cannot be removed by gauge transformations, or, equivalently by varying local spin axes. This brings frustrations to magnetic properties. To obtain a qualitative understanding, two different limits of $|\lambda| \ll |t|$ and $|\lambda| \gg |t|$ will be considered.

In the absence of the SO coupling, i.e. $\lambda = 0$, the system is in the ferromagnetic state. If λ is small, the J_2 -term brings the easy plane anisotropy which prefers spin moments lie in the xy -plane. The DM vector further induces spin spiraling at a finite

wavevector, which can be shown by calculating the spin-wave spectra around the variational ground states that spin moments lie along the high symmetry line of diagonal directions, say, $[\bar{1}\bar{1}0]$. The Holstein–Primakoff transformation is employed to transform equation (50) into the magnon Hamiltonian,

$$H_{\text{mg}} = -J_0 \sum_i \left\{ \left(\cos 2\theta - i \frac{\sin 2\theta}{\sqrt{2}} \right) a_i^\dagger a_{i+e_x} + \left(\cos 2\theta + i \frac{\sin 2\theta}{\sqrt{2}} \right) a_i^\dagger a_{i+e_y} + \text{h.c.} \right\}, \quad (52)$$

where a^\dagger is the creation operator for magnons deviating from the $[110]$ -direction and $\theta = \arctan(\lambda/t)$ as defined above. We only keep quadric terms and ignore the terms proportional to $\sin^2 \theta$ since $\lambda/t \ll 1$. In momentum space, its spectra can be diagonalized as

$$\epsilon(\vec{k}) = -2J_0 \left\{ \cos 2\theta (\cos k_x + \cos k_y) + \frac{1}{\sqrt{2}} \sin 2\theta (\sin k_x - \sin k_y) \right\}, \quad (53)$$

whose minima are located at $\vec{Q}_M = (2k, -2k)$ with the value of k given in equation (49). This indicates that the ground state exhibits a spin-spiral order along the direction perpendicular to the quantized axis in the spin-wave analysis.

Interestingly, in the opposite limit of $|\lambda/t| \gg 1$, equation (51) can be related to that of $|\lambda/t| \ll 1$ through a duality transformation. On site i with the coordinates (i_x, i_y) , \vec{S}_i is transformed into

$$\begin{aligned} S_{i_x, i_y}^x &\rightarrow (-1)^{i_x} S_{i_x, i_y}^x; & S_{i_x, i_y}^y &\rightarrow (-1)^{i_y} S_{i_x, i_y}^y; \\ S_{i_x, i_y}^z &\rightarrow (-1)^{i_x + i_y} S_{i_x, i_y}^z. \end{aligned} \quad (54)$$

\vec{S}_i still maintains the spin commutation relation. Under this transformation, the J_1 -term transforms into the J_2 -term and vice versa, and the J_{12} -term is invariant. Thus this dual transformation indicates that there is a one-to-one correspondence between the J_2 -dominant phase ($|\lambda/t| \gg 1$) and that of J_1 with $|\lambda/t| \ll 1$ which has been analysed above.

In the regime of intermediate values λ/t , a rich phase diagram with different spin patterns appears. Classical Monte Carlo simulations have been employed to calculate the ground state phase diagram in current literatures [92–94]. Various patterns have been found as a result of competition among ferromagnetic exchange, easy-plane anisotropy and the DM-effect-induced spin spirals. These include the ferromagnetic, antiferromagnetic, spiral, stripes and vortex crystal orderings. Furthermore, the superfluid–insulator transition for SO-coupled bosons has been studied in [95]. And a similar topic in the presence of both SO coupling and effective magnetic fields has also been considered in [96].

7. Conclusions

We have reviewed unconventional BECs with SO coupling whose condensate wavefunctions are complex-valued and are thus beyond the framework of the ‘no-node’ theorem. Even at the single-particle level, the spectra in harmonic traps exhibit

the structure of Landau-level-like quantization induced by SO couplings. Their energy dispersion is nearly flat with respect to angular momentum in the case of strong SO coupling, and exhibit the Z_2 -type topology. The interacting condensates exhibit topologically non-trivial configurations. In the 2D Rashba case, the spin density distributions are characterized by the skyrmion-type textures. The 3D Weyl SO coupling induces the topological phase defects in the quaternionic phase space, and the corresponding spin density distributions are also non-trivial carrying non-zero values of the Hopf invariant. In rotating traps, the condensate configurations are changed by vorticity which results in a variety of structures including skyrmion lattices, giant vortices, multi-domains of plane-waves. In the strongly correlated Mott-insulating states, the SO coupling exhibits the DM exchange interactions in the quantum magnetism. The research of novel states of SO-coupled bosons is still in the early stage. In particular, the effect of SO couplings in the strong correlation regime is still a largely unexplored field. We expect that further exciting progress on the novel states of SO-coupled bosons will appear in the near future.

Acknowledgments

The authors thank L Butov, T L Ho, H Hu, H Pu, T Xiang, C W Zhang, F Zhou, B F Zhu and I Mondragon-Shem for helpful discussions. XFZ acknowledges the support by NSFC (grant no. 11004186), National Basic Research Program of China 2011CB921204, and the Strategic Priority Research Program of the Chinese Academy of Sciences (grant no. XDB01000000). YL and CW are supported by the NSF DMR-1105945 and AFOSR FA9550-11-1-0067(YIP); YL is also supported by the Inamori Fellowship. ZC acknowledges funding by DFG FOR 801.

References

- [1] Žutić I, Fabian J and Sarma S D 2004 *Rev. Mod. Phys.* **76** 323
- [2] Nagaosa N *et al* 2010 *Rev. Mod. Phys.* **82** 1539
- [3] Xiao D, Chang M-C and Niu Q 2010 *Rev. Mod. Phys.* **82** 1959
- [4] D'yakonov M and Perel V 1971 *Sov. Phys.—JETP Lett.* **13** 467
- [5] Hirsch J E 1999 *Phys. Rev. Lett.* **83** 1834
- [6] Murakami S, Nagaosa N and Zhang S-C 2003 *Science* **301** 1348
- [7] Sinova J *et al* 2004 *Phys. Rev. Lett.* **92** 126603
- [8] Hasan M Z and Kane C L 2010 *Rev. Mod. Phys.* **82** 3045
- [9] Qi X-L and Zhang S-C 2011 *Rev. Mod. Phys.* **83** 1057
- [10] Galitski V and Spielman I B 2013 *Nature* **494** 49–54
- [11] Lin Y *et al* 2009 *Nature* **462** 628
- [12] Lin Y *et al* 2009 *Phys. Rev. Lett.* **102** 130401
- [13] Lin Y, Jimenez-Garcia K and Spielman I 2011 *Nature* **471** 83
- [14] Zhang J *et al* 2012 *Phys. Rev. Lett.* **109** 115301
- [15] Wang P *et al* 2012 *Phys. Rev. Lett.* **109** 095301
- [16] Qu C *et al* 2013 arXiv:1301.0658
- [17] Cheuk L W *et al* 2012 *Phys. Rev. Lett.* **109** 095302
- [18] Feynman R P 1972 *Statistical Mechanics, A Set of Lectures* (Reading, MA: Addison-Wesley)
- [19] Wu C 2009 *Mod. Phys. Lett. B* **23** 1
- [20] Isacsson A and Girvin S M 2005 *Phys. Rev. A* **72** 053604
- [21] Liu W V and Wu C 2006 *Phys. Rev. A* **74** 013607
- [22] Kuklov A B 2006 *Phys. Rev. Lett.* **97** 110405
- [23] Cai Z and Wu C 2011 *Phys. Rev. A* **84** 033635
- [24] Müller T, Fölling S, Widera A and Bloch I 2007 *Phys. Rev. Lett.* **99** 200405
- [25] Wirth G, Ölschläger M and Hemmerich A 2010 *Nature Phys.* **7** 147
- [26] Ölschläger M, Wirth G and Hemmerich A 2011 *Phys. Rev. Lett.* **106** 015302
- [27] Wu C and Mondragon-Shem I 2008 arXiv:0809.3532V1
Wu C, Mondragon-Shem I and Zhou X-F 2011 *Chin. Phys. Lett.* **28** 097102
- [28] Stanescu T D, Anderson B and Galitski V 2008 *Phys. Rev. A* **78** 023616
- [29] Jaksch D and Zoller P 2003 *New J. Phys.* **5** 56
- [30] Ruseckas J, Juzeliūnas G, Öhberg P and Fleischhauer M 2005 *Phys. Rev. Lett.* **95** 010404
- [31] Osterloh K *et al* 2005 *Phys. Rev. Lett.* **95** 010403
- [32] Liu X-J, Borunda M F, Liu X and Sinova J 2009 *Phys. Rev. Lett.* **102** 046402
- [33] Campbell D L, Juzeliūnas G and Spielman I B 2011 *Phys. Rev. A* **84** 025602
- [34] Juzeliūnas G, Ruseckas J, Campbell D and Spielman I 2011 *Proc. SPIE* **7950** 79500M
- [35] Dalibard J, Gerbier F, Juzeliūnas G and Öhberg P 2011 *Rev. Mod. Phys.* **83** 1523
- [36] Tagliacozzo L, Celi A, Orland P and Lewenstein M 2012 arXiv:1211.2704
- [37] Goldman N, Gerbier F and Lewenstein M 2013 arXiv:1301.4959v1
- [38] Wang C, Gao C, Jian C and Zhai H 2010 *Phys. Rev. Lett.* **105** 160403
- [39] Ho T and Zhang S 2011 *Phys. Rev. Lett.* **107** 150403
- [40] Anderson B, Taylor J and Galitski V 2011 *Phys. Rev. A* **83** 031602
- [41] Burrello M and Trombettoni A 2010 *Phys. Rev. Lett.* **105** 125304
- [42] Burrello M and Trombettoni A 2011 *Phys. Rev. A* **84** 043625
- [43] Kawakami T, Mizushima T and Machida K 2011 *Phys. Rev. A* **84** 011607
- [44] Li Y and Wu C 2011 arXiv:1103.5422
- [45] Sinha S, Nath R and Santos L 2011 *Phys. Rev. Lett.* **107** 270401
- [46] Xu Z F, Lü R and You L 2011 *Phys. Rev. A* **83** 053602
- [47] Yip S-K 2011 *Phys. Rev. A* **83** 043616
- [48] Zhu Q, Zhang C and Wu B 2011 arXiv:1109.5811
- [49] Barnett R *et al* 2012 *Phys. Rev. A* **85** 023615
- [50] Deng Y *et al* 2012 *Phys. Rev. Lett.* **108** 125301
- [51] Graß T, Juliá-Díaz B and Lewenstein M 2012 arXiv:1210.8035
- [52] He P, Liao R and Liu W 2012 *Phys. Rev. A* **86** 043632
- [53] Hu H, Ramachandran B, Pu H and Liu X 2012 *Phys. Rev. Lett.* **108** 10402
- [54] Li Y, Pitaevskii L and Stringari S 2012 *Phys. Rev. Lett.* **108** 225301
- [55] Ramachandran B *et al* 2012 *Phys. Rev. A* **85** 023606
- [56] Ruokokoski E, Huhtamäki J and Möttönen M 2012 arXiv:1205.4601
- [57] Sedrakyan T, Kamenev A and Glazman L 2012 arXiv:1208.6266
- [58] Xu X and Han J 2012 *Phys. Rev. Lett.* **108** 185301
- [59] Xu Z, Kawaguchi Y, You L and Ueda M 2012 *Phys. Rev. A* **86** 033628
- [60] Zhang D, Fu L, Wang Z and Zhu S 2012 *Phys. Rev. A* **85** 043609
- [61] Zhang X *et al* 2012 *Phys. Rev. A* **86** 063628
- [62] Zhang Y, Mao L and Zhang C 2012 *Phys. Rev. Lett.* **108** 35302
- [63] Zheng W and Li Z 2012 *Phys. Rev. A* **85** 053607
- [64] Cui X and Zhou Q 2012 arXiv:1206.5918
- [65] Li Y, Zhou X and Wu C 2012 *Phys. Rev. B* **85** 125122
- [66] Anderson B M, Juzeliūnas G, Galitski V M and Spielman I B 2012 *Phys. Rev. Lett.* **108** 235301

- [67] Anderson B and Clark C 2012 arXiv:[1206.0018](#)
- [68] Bermudez A, Mazza L, Rizzi M, Goldman N, Lewenstein M and Martin-Delgado M A 2010 *Phys. Rev. Lett.* **105** 190404
- [69] Yang M and Zhu S-L 2010 *Phys. Rev. A* **82** 064102
- [70] Xu Z-F and You L 2012 *Phys. Rev. A* **85** 043605
- [71] Weyl H 1929 *Z. Phys.* **56** 330
- [72] Li Y, Zhou X and Wu C 2012 arXiv:[1205.2162](#)
- [73] Kawakami T, Mizushima T, Nitta M and Machida K 2012 *Phys. Rev. Lett.* **109** 015301
- [74] Cui X 2012 *Phys. Rev. A* **85** 022705
- [75] Vyasankere J P and Shenoy V B 2012 *New J. Phys.* **14** 043041
- [76] Zhang D-W *et al* 2013 arXiv:[1301.2869](#)
- [77] Yao W and Niu Q 2008 *Phys. Rev. Lett.* **101** 106401
- [78] High A *et al* 2011 arXiv:[1103.0321](#)
- [79] High A *et al* 2012 *Nature* **483** 584–8
- [80] Ghosh S K, Vyasankere J P and Shenoy V B 2011 *Phys. Rev. A* **84** 053629
- [81] Radić J, Sedrakyan T, Spielman I and Galitski V 2011 *Phys. Rev. A* **84** 063604
- [82] Xu X and Han J 2011 *Phys. Rev. Lett.* **107** 200401
- [83] Liu C and Liu W 2012 *Phys. Rev. A* **86** 033602
- [84] Zhao Y, An J and Gong C 2013 *Phys. Rev. A* **87** 013605
- [85] Zhou X, Zhou J and Wu C 2011 *Phys. Rev. A* **84** 063624
- [86] Ramachandran B, Hu H and Pu H 2013 arXiv:[1301.0800v1](#)
- [87] Graß T, Juliá-Díaz B, Barberán N and Lewenstein M 2012 *Phys. Rev. A* **86** 021603
- [88] Graß T, Juliá-Díaz B and Lewenstein M 2012 arXiv:[1210.8035](#)
- [89] Palmer R N and Pachos J K 2011 *New J. Phys.* **13** 065002
- [90] Komineas S and Cooper N R 2012 *Phys. Rev. A* **85** 053623
- [91] Cai Z, Zhou X and Wu C 2012 *Phys. Rev. A* **85** 061605
- [92] Cole W, Zhang S, Paramekanti A and Trivedi N 2012 *Phys. Rev. Lett.* **109** 85302
- [93] Radić J, Di Ciolo A, Sun K and Galitski V 2012 *Phys. Rev. Lett.* **109** 85303
- [94] Gong M, Qian Y, Scarola V and Zhang C 2012 arXiv:[1205.6211](#)
- [95] Mandal S, Saha K and Sengupta K 2012 arXiv:[1205.3178](#)
- [96] Graß T, Saha K, Sengupta K and Lewenstein M B 2011 *Phys. Rev. A* **84** 053632
- [97] Iskin M and Subaşı A 2011 *Phys. Rev. Lett.* **107** 50402
- [98] Jiang L, Liu X, Hu H and Pu H 2011 *Phys. Rev. A* **84** 063618
- [99] Zhou J, Zhang W and Yi W 2011 *Phys. Rev. A* **84** 063603
- [100] Doko E, Subaşı A and Iskin M 2012 *Phys. Rev. A* **85** 053634
- [101] He L and Huang X 2012 *Phys. Rev. Lett.* **108** 145302
- [102] He L and Huang X 2012 arXiv:[1207.2810](#)
- [103] Hu H *et al* 2012 arXiv:[1208.5841](#)
- [104] Liu X 2012 *Phys. Rev. A* **86** 033613
- [105] Maldonado-Mundo D, Ohberg P and Valiente M 2012 arXiv:[1212.3565](#)
- [106] Martone G, Li Y, Pitaevskii L and Stringari S 2012 *Phys. Rev. A* **86** 063621
- [107] Orth P *et al* 2012 arXiv:[1212.5607](#)
- [108] Vyasankere J and Shenoy V 2012 arXiv:[1201.5332](#)
- [109] Zhang S, Yu X, Ye J and Liu W 2012 arXiv:[1212.0424](#)
- [110] Li Y, Zhang S-C and Wu C 2012 arXiv:[1208.1562](#)
- [111] Li Y, Intriligator K, Yu Y and Wu C 2012 *Phys. Rev. B* **85** 085132
- [112] Halperin B I 1982 *Phys. Rev. B* **25** 2185
- [113] Kane C L and Mele E J 2005 *Phys. Rev. Lett.* **95** 146802
- [114] Fu L and Kane C L 2007 *Phys. Rev. B* **76** 045302
- [115] Moore J E and Balents L 2007 *Phys. Rev. B* **75** 121306
- [116] Roy R 2010 *New J. Phys.* **12** 065009
- [117] Zhou F 2003 *Int. J. Mod. Phys. B* **17** 2643
- [118] Mueller E J 2004 *Phys. Rev. A* **69** 033606
- [119] Mueller E J 2004 *Phys. Rev. A* **70** 041603
- [120] Adler S 1995 *Quaternionic Quantum Mechanics and Quantum Fields* vol 88 (New York: Oxford University Press)
- [121] Finkelstein D, Jauch J, Schiminovich S and Speiser D 1962 *J. Math. Phys.* **3** 207
- [122] Balatsky A 1992 arXiv:[cond-mat/9205006](#)
- [123] Wilczek F and Zee A 1983 *Phys. Rev. Lett.* **51** 2250
- [124] Nakahara M 2003 *Geometry, Topology and Physics* (London: Taylor and Francis)
- [125] Kitaev A Y 2003 *Ann. Phys.* **303** 2–30
- [126] Nayak C, Simon S H, Stern A, Freedman M and Sarma S D 2008 *Rev. Mod. Phys.* **80** 1083
- [127] Aidelsburger M *et al* 2011 *Phys. Rev. Lett.* **107** 255301
- [128] Struck J *et al* 2012 *Phys. Rev. Lett.* **108** 225304
- [129] Jiménez-García K *et al* 2012 *Phys. Rev. Lett.* **108** 225303
- [130] Dzyaloshinsky I 1958 *J. Phys. Chem. Solids* **4** 241
- [131] Moriya T 1960 *Phys. Rev.* **120** 91
- [132] Coffey D, Rice T M and Zhang F C 1991 *Phys. Rev. B* **44** 10112
- [133] Bonesteel N E 1993 *Phys. Rev. B* **47** 11302